ABSTRACT

Title of dissertation: HIGH-INTENSITY LASER-MATTER INTERACTIONS
PHYSICS AND APPLICATIONS

Zachary Epstein
Doctor of Philosophy, 2019

Dissertation directed by: Professor Phillip Sprangle
Department of Physics

This dissertation consists of three distinct research topics which involve high-intensity laser-matter interactions. The topics are (1) High-Power Supercontinuum IR Generation, (2) Spectral Broadening of the NIKE KrF Laser in a Negative Nonlinear Index Medium, and (3) Remote Optical Magnetometry.

(1) High-average power, ultra-broadband, mid-IR radiation can be generated by illuminating a nonlinear medium with a multi-line laser radiation. Propagation of a multi-line, pulsed CO_2 laser beam in a nonlinear medium, e.g. gallium arsenide or chalcogenide, can generate directed, broadband, IR radiation in the atmospheric window (2 – 13 μm). A 3-D laser code for propagation in a nonlinear medium has been developed to incorporate extreme spectral broadening resulting from the beating of several wavelengths. The code has the capability to treat coupled forward and backward propagating waves, as well as transverse and full linear dispersion effects. Methods for enhancing the spectral broadening are proposed and analyzed. Grading the refractive index radially or using a cladding will tend to guide the CO_2 radiation

and extend the interaction distance, allowing for enhanced spectral broadening. Nonlinear coupling of the CO_2 laser beam to a backwards-propagating, reflected beam can increase the rate of spectral broadening in the anomalous dispersion regime of a medium. Laser phase noise associated with the finite CO_2 linewidths can significantly enhance the spectral broadening as well. In a dispersive medium laser phase noise results in laser intensity fluctuations. These intensity fluctuations result in spectral broadening due to the self-phase modulation mechanism. Finally, we present propagation through a chalcogenide fiber as an alternative for extreme spectral broadening of a frequency-doubled CO_2 multi-line laser beam.

(2) In inertial confinement (ICF) experiments at the NIKE [1] laser facility, the high-power krypton fluoride (KrF) laser output beams propagate through long ($\sim$75m) air paths to achieve angular multiplexing. This is required because the KrF medium does not store energy for a sufficiently long time. Recent experiments and simulations have shown that, via stimulated rotational Raman scattering (SRRS), this propagation can spectrally broaden the laser beam well beyond the $\sim$1 THz laser linewidth normally achieved by the induced spatial incoherence (ISI) technique used in NIKE [2]. These enhanced bandwidths may be enough to suppress the laser-plasma instabilities which limit the maximum intensity that can be incident on the ICF target. We investigate an alternative technique that achieves spectral broadening by self-phase modulation in Xe gas, which has a large, negative nonlinear refractive index $\sim$ 248 nm [3], and thus completely avoids transverse filamentation issues. The collective, nonlinear atomic response to the chaotic, non-steady state ISI light is modeled using a two-photon vector model. The effect of near-resonant behavior on the spectral broadening is also studied.

(3) Here we analyze a mechanism for remote optical measurements of magnetic field vari-

ations above the surface of seawater. This magnetometry mechanism is based on the polarization rotation of reflected polarized laser light, in the presence of the earth's magnetic field. Here the laser light is reflected off the surface of the water and off an underwater object. Two mechanisms responsible for the polarization rotation are the Surface Magneto-Optical Kerr Effect (SMOKE) and the Faraday effect. In both mechanisms the degree of polarization rotation is proportional to the earth's local magnetic field. Variations in the earth's magnetic field due to an underwater object will result in variations in the polarization rotation of the laser light reflected off the water's surface (SMOKE) and off the underwater object (Faraday effect). An analytical expression is obtained for the polarization-rotated field when the incident plane wave is at arbitrary angle and polarization with respect to the water's surface. We find that the polarization rotated field due to SMOKE is small compared to that due to the Faraday effect.

HIGH-INTENSITY LASER-MATTER INTERACTIONS PHYSICS AND APPLICATIONS

by

Zachary Epstein

Dissertation submitted to the Faculty of the Graduate School of the
University of Maryland, College Park in partial fulfillment
of the requirements for the degree of
Doctor of Philosophy
2019

Advisory Committee:
Professor Phillip Sprangle[1,2], Chair/Advisor
Professor Thomas Antonsen[1]
Professor Howard Milchberg[1]
Dr. Joseph Peñano[2]
Dr. Robert Lehmberg[2]
Professor Rajarshi Roy[1] (Dean's Representative)

[1]University of Maryland, College Park, MD 20742-4111
[2]Plasma Physics Division, Naval Research Laboratory, Washington DC 20375

Acknowledgments

My thesis was made possible by the guidance and contributions of many individuals.

(i) I'd first like to thank Professor Phillip Sprangle for being an extraordinary advisor and mentor. He granted me the opportunity to work on interesting, challenging, and applicable projects, made himself very available, and offered advice and guidance throughout the process. It has been a pleasure to work with and learn from him, from the day five years ago when I arranged a meeting with him to chat about his career and which strategies he used to make such large contributions to science and to the country.

(ii) I would also like to thank Dr. Robert Lehmberg, Professor Antonio Ting, Dr. Luke Johnson, Dr. Joseph Penano, and Dr. Bahman Hafizi for many fruitful discussions and for their guidance. I am grateful to Professors Howard Milchberg and Thomas Antonsen for agreeing to serve on my thesis committee and for making it a pleasure to work in the department.

(iii) My office mates have enriched my graduate life in many ways and deserve a special mention - Joshua Isaacs, Luke Johnson, Chenlong Miao, Thomas Rensink, Evan Dowling, and Paul Gradney. It has been a lot of fun sharing an office with you all.

(iv) I would like to acknowledge help and support from the IREAP staff members. In particular, Ed Condon's computer hardware help was highly appreciated, and Leslie Delabar made it a breeze to navigate involved technical issues.

(v) I would also like to acknowledge the Office of Naval Research for funding the work contained in this dissertation and in particular Quentin Saulter ONR USPL PM.

(vi) Thank you to my wife Nadine for her patience, love, warmth, energy, support, and mesiras nefesh, and for being a true tzadekkes throughout the entire PhD.

(vii) Thank you to my parents for instilling within the me strength to make it through graduate school while balancing a wide range of priorities, and for supporting me through every step of my education.

(viii) I would like to acknowledge financial support from ONR, NEEC, and NRL for the various projects discussed in this dissertation.

Contents

List of Figures

List of Tables

Part I

Introduction

This dissertation consists of three topics which involve high-intensity laser-matter interactions. Involvement in several projects has enabled a broader understanding of the fields. The topics are (1) High-Power Supercontinuum IR Generation, (2) Spectral Broadening of the NIKE KrF Laser in a Negative Nonlinear Index Medium, and (3) Remote Optical Magnetometry. The main two topics - (1) and (2) - both have the goal of spectrally broadening a laser, albeit under very different circumstances for different applications.

Topics (1) and (3) were published as first-author peer-reviewed publications in JOSA B and IEEE Quantum Electronics, respectively, and the third topic will be submitted to Physical Review E this month for peer review. In addition, numerous presentations have been made involving content of this dissertation (see List of Publications and Presentations).

The first research topic involves the generation of high-power ultra-broadband mid-IR radiation, which is relevant to the remote detection of chemicals and to IR countermeasures, and can be achieved by beating together two CO_2 laser lines and propagating the resulting beam through a GaAs crystal. Previously, supercontinuum IR radiation up in the 0.1-1 kW average IR power regime had been analytically and numerically studied only in 1D (see Ref. [5-6] of Part 1). A 3D bi-directional code (BTUL) was developed with the capability to treat extreme spectral bandwidths and coupling between forward and backward waves. It also includes all $\chi^{(1)}$ effects (group velocity dispersion, third-order dispersion, etc) and $\chi^{(3)}$ effects (self-phase modulation, four-wave mixing, cross-phase modulation, third harmonic generation,

etc), as well as spatial variations in the linear refractive index. Three methods are proposed and analyzed to enhance spectral broadening: i) radially grading the linear refractive index, ii) coupling to a backwards-propagating, reflected wave, and iii) taking advantage of laser phase noise. Spectral broadening in a chalcogenide fiber is considered as well.

The second research topic involves the spectral broadening of KrF laser light in Xe, which has a large, negative nonlinear index at the 248.4 nm laser wavelength due to a two-photon resonance at 249.6 nm. The research is relevant to inertial confinement fusion, in which a large bandwidth can mitigate laser plasma instabilities and cross beam transfer. In particular, the Naval Research Laboratory's NIKE KrF laser beams propagate across distances of tens of meters, over which spectral broadening in a tube of Xe gas is a possibility. The negative value of the nonlinear index is an ideal property because it precludes the occurrence of laser beam breakup. Spectral broadening and beam profile degradation in Xe are quantified and simulated, and the effect of the initial times-diffraction-limited value (M_X^2) on these quantities is found to be significant.

The third research topic involves two mechanisms for detecting variations in the Earth's magnetic field due to underwater objects. It is found that reflecting polarized light off the surface of seawater results in two contributions of polarization-rotated light. The first is a purely surface effect called the Surface Magneto-Optical Kerr Effect (SMOKE) which turns out to be small. The latter contribution is a volume effect - the Faraday effect. The contribution from the Faraday effect can be significant but is only relevant to shallow ($\sim$ 10m depth) objects. The contribution of SMOKE is analyzed for arbitrary polarization direction, incident angle, and magnetic field direction.

Part II

High-Power Supercontinuum IR Generation

High-average power, ultra-broadband, mid-IR radiation can be generated by illuminating a nonlinear medium with a multi-line laser radiation. Propagation of a multi-line, pulsed CO_2 laser beam in a nonlinear medium, e.g. gallium arsenide or chalcogenide, can generate directed, broadband, IR radiation in the atmospheric window (2 – 13 μm). A 3-D laser code for propagation in a nonlinear medium has been developed to incorporate extreme spectral broadening resulting from the beating of several wavelengths. The code has the capability to treat coupled forward and backward propagating waves, as well as transverse and full linear dispersion effects. Methods for enhancing the spectral broadening are proposed and analyzed. Grading the refractive index radially or using a cladding will tend to guide the CO_2 radiation and extend the interaction distance, allowing for enhanced spectral broadening. Nonlinear coupling of the CO_2 laser beam to a backwards-propagating, reflected beam can increase the rate of spectral broadening in the anomalous dispersion regime of a medium. Laser phase noise associated with the finite CO_2 linewidths can significantly enhance the spectral broadening as well. In a dispersive medium laser phase noise results in laser intensity fluctuations. These intensity fluctuations result in spectral broadening due to the self-phase modulation mechanism. Finally, we present propagation through a chalcogenide fiber as an alternative for extreme spectral broadening of a frequency-doubled CO_2 multi-line laser beam.

1 Introduction

High-average power and high peak power, ultra-broadband radiation sources in the long-wave (8 – 13 μm) and mid-wave (2 – 5 μm) infrared regime have applications for remote sensing and IR countermeasures. The generation of a mid-IR ultra-broadband (supercontinuum) source was demonstrated using a 3ps CO_2 laser pulse with GW peak power propagating through GaAs [1]. For higher average powers (up to ∼100 mW), there are ongoing experiments and modeling efforts at UCLA. In one experiment, a train of seven interspersed 3 ps pulses with GW peak power was propagated through GaAs just below the breakdown intensity, i.e., ∼10 GW/cm^2 [2]. Another experiment [3] employed a 200 ps , CO_2 pulse train operating at a peak power of 150 MW and consisting of consecutive, ∼10 ps micropulses just below the breakdown intensity of GaAs, i.e., ∼1 GW/cm^2 for pulses far exceeding 1 ps. In these experiments it was observed that second order nonlinear processes restrictively affected the supercontinuum generation. Elimination of the second order nonlinear effect via selecting the appropriate orientation of GaAs may enable the generation of an efficient, pulsed radiation source in the given regime [2 – 4].

Supercontinuum IR radiation in the 0.1 – 1 kW average IR power regime in GaAs has been analytically and numerically studied in 1D [5 – 6]. In these early theoretical studies a spectrum spanning the mid-IR regime was generated by the beating of two lines of CO_2 radiation in GaAs. The intensity of each line was 250 MW/cm^2, and the resulting spectrum covered ∼ 5 – 16 μm after propagating 7.8 cm in GaAs. However, transverse effects and surface damage thresholds were not considered. The simulations were based on the 1D Nonlinear Schrodinger Equation (NLSE) model which is only valid when the fractional frequency spread is somewhat

less than unity.

Our formulation of the spectral broadening process allows for fractional frequency spreads approaching unity and coupling to a backwards-propagating beam. In addition, we include transverse and full linear dispersion effects, and methods for enhancing the spectral broadening are proposed and analyzed.

Ultra-broad band radiation can be generated by a number of coupled nonlinear optical processes [1, 7] which occur in certain material, e.g., GaAs, when illuminated by multi-lined CO_2 radiation. To cover the entire IR atmospheric transmission windows (8 – 13 μm) and (2 – 5 μm) the CO_2 laser would operate at both the fundamental and second harmonic.

The dominant interrelated nonlinear processes include: i) self-phase modulation, ii) 4-wave mixing, iii) cross-phase modulation, iv) stimulated Raman scattering and v) stimulated Brillouin scattering. These processes can lead to wide spectral broadening of the lines around the fundamental ($\sim$ 10 μm) and second harmonic ($\sim$ 5 μm) with high conversion efficiencies. These mechanisms have the flexibility of adjustable spectral widths. A schematic of the concept is shown in Fig. 1.

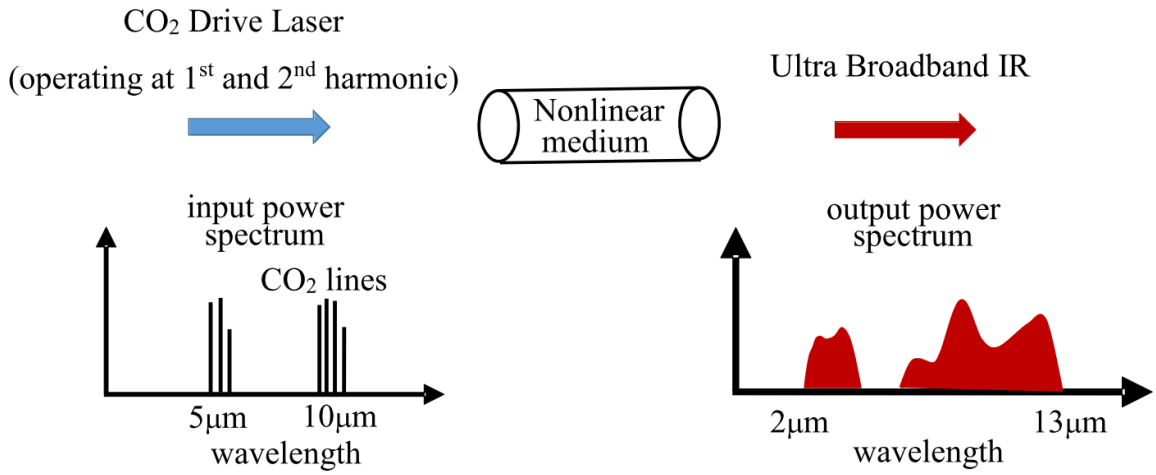

Figure 1: A schematic of the concept showing the output spectrum extending from 2 – 13 μm.

2 Propagation and Interaction Model

The wave equations which form the basis of the Bi-directional, Three-dimensional, Ultra-broadband Laser (BTUL) code are obtained in this section. This code will be used to simulate supercontinuum generation and self-focusing.

2.1 Nonlinear Propagation Code

By taking the electric field to be linearly polarized along the x-axis, and neglecting free charges and coupling to polarization-rotated fields (arising from the divergence term), the electric field in a spatially inhomogenous medium is given by the wave equation

$$\nabla^2 E(\mathbf{r},t) - \frac{1}{c^2}\frac{\partial^2}{\partial t^2}E(\mathbf{r},t) = \mu_0 \frac{\partial^2}{\partial t^2}\left(P_L(\mathbf{r},t) + P_{NL}(\mathbf{r},t)\right) + \frac{\partial^2}{\partial x^2}E(\mathbf{r},t)\ , \tag{1}$$

where the last term emerges from the divergence term $\vec{\nabla}\left(\vec{\nabla}\cdot\mathbf{E}(\mathbf{r},t)\right)$, and where $E(\mathbf{r},t) = (1/2)\hat{E}(\mathbf{r},t)\exp\left(i(k_0 z - \omega_0 t)\right) + c.c.$ is the electric field, $\hat{E}(\mathbf{r},t)$ is the complex amplitude, ω_0 is the carrier frequency, $k_0 = n_L(\omega_0)\omega_0/c$ is the carrier wavenumber, $n_L(\omega)$ is the linear refractive index, and $P_L(\mathbf{r},t)$ and $P_{NL}(\mathbf{r},t)$ are respectively, the linear and nonlinear polarization fields. In Eq. (1), The term $(\partial/\partial y)\left(\vec{\nabla}\cdot\mathbf{E}(\mathbf{r},t)\right)$ is absent in Eq. (1) because it drives the field along the y-axis.

Using the relation $\nabla\cdot(n^2(\mathbf{r},t)E(\mathbf{r},t)) = \rho_f$, where $\rho_f = 0$ is the free charge density, the divergence term in Eq. (1) can be written as,

$$\vec{\nabla}\cdot\vec{E}(\mathbf{r},t)=\left(-\vec{E}(\mathbf{r},t)\cdot\frac{\nabla n^2(\mathbf{r},t)}{n^2(\mathbf{r},t)}\right)=\left(-E(\mathbf{r},t)\frac{\partial}{\partial x}\ln\big(n^2(\mathbf{r},t)\big)\right)$$
$$\approx-\frac{2E(\mathbf{r},t)}{n_{L0}}\frac{\partial}{\partial x}(\delta n_L(\mathbf{r})+\delta n_{NL}(\mathbf{r},t)) \tag{2}$$

where $n(\mathbf{r},t)=n_{L0}+\delta n_L(\mathbf{r})+\delta n_{NL}(\mathbf{r},t)$, n_{L0} is the linear refractive index of the medium, and $\delta n_L(\mathbf{r})$ and $\delta n_{NL}(\mathbf{r},t)$ are respectively, linear and nonlinear variations in the refractive index of the (spatially-varying) medium. We express the latter term as $\delta n_{NL}(\mathbf{r},t)=n_2 n_{L0}\varepsilon_0 c|E(\mathbf{r},t)|^2/2$, where n_2 represents the Kerr effect. Terms of the form $(\partial/\partial y)$ do not appear in Eq. (2) since the electric field is x-polarized. Because the beam is smooth with spot size $R_0\gg\lambda_0$, the divergence term is small for a linear refractive index that is constant or weakly varying in space. Its treatment will be discussed at the end of this section.

Taking the Fourier transform (neglecting the divergence term) of Eq. (1) in time and transverse space yields the following equation,

$$\left(\frac{\partial^2}{\partial z^2}+k_z^2\right)\tilde{E}(k_x,k_y,z,\omega)=-\mu_0\omega^2\tilde{P}_{NL}(k_x,k_y,z,\omega), \tag{3}$$

where $k_z^2=k^2(\omega)-k_x^2-k_y^2$, $k(\omega)=n_L(\omega)\omega/c$ and k_x, k_y denote transverse spatial frequencies. In obtaining Eq. (3) the Fourier transforms are defined as $\tilde{Q}(k_x,k_y,z,\omega)=\iiint Q(\mathbf{r},t)\times\exp\left(i(\omega t-k_x x-k_y y)\right)\mathrm{d}t\mathrm{d}x\mathrm{d}y$ and the transform of the linear polarization field is $\tilde{P}_L(k_x,k_y,z,\omega)=\varepsilon_0\chi_L(\omega)\tilde{E}(k_x,k_y,z,\omega)$ where $n_L(\omega)=\sqrt{1+\chi_L(\omega)}$ and χ_L is the linear susceptibility.

In the case of an instantaneous nonlinear Kerr response, the nonlinear polarization field in

Eq. (3) can be written as

$$\tilde{P}_{NL}(k_x, k_y, z, \omega) = \varepsilon_0 \chi_{NL}(\omega) \iiint E(\mathbf{r}, t) E(\mathbf{r}, t) E(\mathbf{r}, t) \exp\left(i(\omega t - k_x x - k_y y)\right) \mathrm{d}t\mathrm{d}x\mathrm{d}y \quad (4)$$

where χ_{NL} is the nonlinear susceptibility, which in general is frequency dependent. The fields in Eq. (4) can be written as the sum of a forward and backward propagating wave, i.e., $\tilde{E} = \tilde{E}^+ + \tilde{E}^-$ and $\tilde{P}_{NL} = \tilde{P}^+_{NL} + \tilde{P}^-_{NL}$. Using this form, Eq. (3) becomes $(\partial/\partial z + ik_z)(\partial/\partial z - ik_z)\tilde{E}^{\pm}(k_x, k_y, z, \omega) = -\mu_0 \omega^2 \tilde{P}^{\pm}_{NL}(k_x, k_y, z, \omega)$. If the backward propagating wave is small compared to the forward propagating wave, $|E^-| \ll |E^+|$, the transform of the nonlinear polarization field is

$$\tilde{P}^+_{NL}(k_x, k_y, z, \omega) = \varepsilon_0 \ \chi_{NL} \iiint \mathrm{d}t\mathrm{d}x\mathrm{d}y \left(E^+(\mathbf{r}, t)\right)^3 \exp\left(i(\omega t - k_x x - k_y y)\right) \quad (5a)$$

$$\tilde{P}^-_{NL}(k_x, k_y, z, \omega) = 3 \ \varepsilon_0 \ \chi_{NL} \iiint \mathrm{d}t\mathrm{d}x\mathrm{d}y \left[\left(E^+(\mathbf{r}, t)\right)^2 E^-(\mathbf{r}, t)\right]_- \exp\left(i(\omega t - k_x x - k_y y)\right). \quad (5b)$$

where the subscript " $-$ " refers to the backwards-propagating component. The general case, in which the backward propagating wave can be significant, is treated in the Supplement. Using the approximation $(\partial/\partial z \pm ik_z)\tilde{E}^{\pm}(k_x, k_y, z, \omega) \approx \pm 2ik_z \tilde{E}^{\pm}(k_x, k_y, z, \omega)$, results in the

final expression

$$\frac{\partial}{\partial z}\tilde{E}^{\pm}(k_x,k_y,z,\omega) = \\ \pm ik_z\tilde{E}^{\pm}(k_x,k_y,z,\omega) \pm \frac{i\mu_0\omega^2}{2k_z}\tilde{P}^{\pm}_{NL}(k_x,k_y,z,\omega). \tag{6}$$

The bi-directional capability of BTUL will enable, for example, study of how coupling to a reflected backwards-propagating wave affects extreme spectral broadening in a nonlinear medium. In the absence of a backward-propagating wave, the BTUL equations reduce to the Unidirectional Pulse Propagation Equation (UPPE) derived in Ref. [8 – 9]. The UPPE allows for simulations of ultra-broadband radiation with dispersion. We note the existence of a generalized UPPE (gUPPE) as given in Ref. [10], which allows for the treatment of a strongly-varying spatial dependence in the linear refractive index, though it does so in the absence of a backwards propagating wave.

A weakly-varying spatial dependence in the linear refractive index may be incorporated by the addition of the term $\pm(i/2k_z)\int \delta k^2(x,y,z,\omega)E^{\pm}(x,y,z,\omega)\exp(-i(k_x x+k_y y))\mathrm{d}x\mathrm{d}y$ to the right-hand side of Eq. (6), where the linear dispersion relation is written as $k^2(x,y,z,\omega) = k^2(\omega)+\delta k^2(x,y,z,\omega)$, $\delta k^2(x,y,z,\omega) \ll k^2(\omega)$. The divergence term in Eq. (2) can be incorporated by the addition of the terms $\pm(i/n_{L0}k_z)\int \frac{\partial}{\partial x}\left(E^{\pm}(x,y,z,\omega)\frac{\partial \delta n_L(\mathbf{r})}{\partial x}\right)\exp\left(-i(k_x x+k_y y)\right)\mathrm{d}x\mathrm{d}y$ and $\pm(i/n_{L0}k_z)\int \frac{\partial}{\partial x}\left(E^{\pm}(x,y,z,t)\frac{\partial \delta n_{NL}(\mathbf{r},t)}{\partial x}\right)\times \exp\left(-i(k_x x+k_y y)+i\omega t\right)\mathrm{d}x\mathrm{d}y\mathrm{d}t$ to the right-hand side of Eq. (6) , where $n_{NL}(\mathbf{r},t) = n_2 I(\mathbf{r},t)$ and the laser intensity time-averaged over several optical cycles is given by $I(\mathbf{r},t) = n_{L0}\varepsilon_0 c\,\langle E(\mathbf{r},t)^2\rangle$.

2.2 Self-Guiding in GaAs Waveguide

In the case of a monochromatic field, the 3D generalization of the nonlinear para-axial envelope equation is

$$\frac{\partial \hat{E}(\mathbf{r})}{\partial z} = \frac{i}{2k_0}\nabla_\perp^2 \hat{E}(\mathbf{r}) + \frac{i}{2k_0}\delta k^2(\mathbf{r})\hat{E}(\mathbf{r}) + i\gamma_0\left|\hat{E}(\mathbf{r})\right|^2 \hat{E}(\mathbf{r}), \tag{7}$$

where the nonlinear coefficient is $\gamma_0 = (3\omega_0/8n_{L0}c)\chi_{NL}(\omega_0) = n_2\omega_0 n_{L0}\varepsilon_0/2$, n_2 represents the Kerr effect, the total refractive index is $n = n_{L0} + \delta n_L + \delta n_{NL}$, $\delta n_{NL} = n_2 I$, and $I = n_{L0}\varepsilon_0 c\left|\hat{E}\right|^2/2$ is the intensity. The term proportional to $\delta k^2(\mathbf{r}) = n_L^2(\mathbf{r})\omega^2/c^2 - k_0^2$ allows for a transverse spatial variation in the linear refractive index, i.e. δn_L. In the case of a GaAs medium, appropriate orientation has been assumed so that second order effects are small.

Representing the complex amplitude of the field in the form $\hat{E}(\mathbf{r}) = A(z)\exp(i\theta(z)) \times \exp(-(1+i\alpha(z))r^2/R^2(z))$, where $r = (x^2+y^2)^{1/2}$, α is related to the radius of curvature of the wavefront, R is the spot size and A and θ are real, Eq. (7) can be written as

$$\begin{aligned} &2ik_0\left(\frac{\partial \ln A}{\partial z} + i\frac{\partial \theta}{\partial z} - i\frac{\partial a}{\partial z}\frac{r^2}{R^2} + 2(1+i\alpha)\frac{r^2}{R^3}\right) \\ &- 4\left(\frac{1+i\alpha}{R^2}\right)\left(1 - \frac{(1+i\alpha)r^2}{R^2}\right) \\ &\approx -\delta k(\mathbf{r}) - 2k_0\gamma_0 A^2(1 - 2r^2/R^2), \end{aligned} \tag{8}$$

where on the right hand side of Eq. (8) the Kerr term has been expanded in r. The radial variation in the linear refractive index is taken to be quadratic in r, i.e., $n_L^2(r,\omega) = n_{L0}^2 + (n_{L0}^2 - 1)r^2/R_C^2$, where R_C is the characteristic radial scale length. Equating powers of r up to r^2 terms and real and imaginary terms in Eq. (8) results in four first order coupled differential

equations for A, θ, α, R: . Combining these equations we find that the laser spot size is given by

$$\frac{\partial^2 R}{\partial z^2} = \frac{4}{k_0^2 R^3}\left(1 - \frac{\mathrm{P}}{\mathrm{P}_K} + \frac{k_0^2(n_{L0}^2 - 1)}{n_{L0}^2}\frac{R^4}{R_C^2}\right), \tag{9}$$

where $\mathrm{P}_K = \lambda_0^2/(8\pi n_{L0} n_2)$ is the nonlinear focusing power and λ_0 is the wavelength in vacuum. A derivation of the laser spot size based on the Source Dependent Expansion method [11 – 12] yields a value for P_K which is 4 times larger than that obtained using the expansion approach in Eq. (8). In the following, we use the correct value of P_K [12]. Simulations over multiple Rayleigh lengths indicate that Eq. (9) is satisfied at low powers for the guiding condition, i.e., $\partial^2 R/\partial z^2 = 0$. It can be shown that the guiding condition is stable with respect to radial perturbations in the spot size. The oscillations of the spot-size perturbations have a longitudinal period given by $\lambda_{\mathrm{osc}} = \sqrt{2}\pi n_{L0} R_C/\sqrt{n_{L0}^2 - 1}$. For typical parameters considered here, λ_{osc} is on the order of cm. In the absence of radial variation in the refractive index, we see from Eq. (9) that the spot size is given by $R(z) = R_0\left(1 + z^2(1 - \mathrm{P}/\mathrm{P}_K)/Z_R^2\right)^{1/2}$, where $Z_R = n_{L0}\pi R_0^2/\lambda_0$ is the Rayleigh length.

To lowest order in the nonlinearity, the field of a beat wave can be written as $E(r,z,t) = E_0 \exp(-r^2/R_0^2)\sum_{\pm}\cos\left((k_0 \pm \Delta k/2)z - (\omega_0 \pm \Delta\omega/2)t\right)$ where $\Delta k = n_{L0}\Delta\omega/c$ and $\Delta\omega \approx 2\pi c\Delta\lambda/\lambda_0^2$. The power in the beat wave is $\mathrm{P}_B(z,t) = \mathrm{P}\cos^2(\Delta k z/2 - \Delta\omega t/2)$ where P is the peak power. The field is now generalized to include the nonlinearity, i.e. $E(r,z,t) \sim \exp\left(-r^2/R^2(z)\right)\exp\left(i(kz - \omega_0 t)\right)$, where $k(z,t) = (n_{L0} + n_{NL})\omega/c = (n_{L0} + n_2 I(z,t))\,\omega/c$ and the on-axis beat wave intensity is $I(z,t) = 2\mathrm{P}_B(z,t)/\left(\pi R^2(z)\right)$. The instantaneous

frequency spread is $\delta\omega \approx -\partial\left(k(z,t)z\right)/\partial t$ and the fractional frequency spread is given by

$$\frac{\delta\omega(z,t)}{\omega_0} \approx \frac{\delta\omega_{\max}(z)}{\omega_0}\sin\left(\Delta kz - \Delta\omega t\right). \tag{10}$$

where

$$\frac{\delta\omega_{\max}(z)}{\omega_0} \approx \frac{1}{2}\left(\frac{\Delta\lambda}{\lambda_0}\right)\left(\frac{z}{Z_R}\right)\left(\frac{\mathrm{P}}{\mathrm{P}_K}\right)\left(\frac{R_0^2}{R^2(z)}\right). \tag{11}$$

Inserting the expression for $R(z)$ into Eq. (11), we find that a laser operating above the nonlinear focusing power and below the breakdown intensity will spectrally broaden and self-focus until the breakdown intensity is reached. For injection below the focusing power and the breakdown intensity, the spectral broadening takes place for the entire length of the medium.

2.3 Longitudinal Modulation Instability of Counterpropagating Beams

Counterpropagating beams can affect one another's modulation instability in the anomalous dispersion regime of a Kerr medium. We have found that the wave vector $K(\omega_m)$ associated with longitudinal instability in the forward-going wave is given by the following dispersion relation:

$$\begin{aligned}(K^2 - K_+^2)(K^2 - K_-^2) - 4\frac{\omega_m^2}{v^2}K^2 \\ = 4\beta_2^2\omega_m^4\Omega_{NL-}\Omega_{NL+} + 2K\frac{\omega_m}{v}(K_+^2 - K_-^2)\ ,\end{aligned} \tag{12}$$

where $K_\pm^2 = \beta_2\omega_m^2(\beta_2\omega_m^2/4 + \Omega_{NL\pm}) - \omega_m^2/v^2$ and $\Omega_{NL\pm} = \chi_{NL}k_0\left|\hat{E}_\pm\right|^2/n_L^2$, where χ_{NL} is the nonlinear susceptibility, n_L is the linear refractive index, $k_0 = n_L\omega_0/c$ is the wave vector associated with the pump frequency ω_0 , β_2 is the group velocity coefficient in the medium at

ω_0 , v is the group velocity , and $\hat{E}_p$ and $\hat{E}_m$ are respectively the forward- and backward-going electric field amplitude.

As will be seen in Section 3.4, coupling to a backward propagating, reflected wave can significantly affect beam propagation in the anomalous dispersion regime of a nonlinear medium.

3 Simulation Results

3.1 Spectral Broadening in GaAs

The parameters used in this study are shown in Table 1. Numerical techniques are discussed in the Supplement.

Table 1: **Parameters used in the spectral broadening examples**

Parameter	Value
Laser wavelength	$\lambda_0 = 9.55$ μm
Laser line separation	$\Delta\lambda/\lambda_0 = 0.01$
Initial spot size	$R_0 = 0.02$ cm
Peak laser power	P = 1.28 MW
Pulse duration	$T \gg 1$ ps
Linear refractive index (GaAs)	$n_{L0} = 3.3$
Nonlinear refractive index (GaAs)	$n_2 = 1.7 \times 10^{-13}$ cm^2/W
Self-focusing power at λ_0	$\mathrm{P}_K = 0.26$ MW
Breakdown intensity	$I_{BD} \sim 0.4$ – 1.5 GW/cm^2

The parameters in Table 1 are applied to all simulations in the paper, unless otherwise specified; in particular, the laser line separation is four times larger in Figures 2b, 3b, 3c, 6, 7, and multiple laser lines are present in Fig. 3c. Figures 6-7 incorporate the $n_L^2(r,\omega) = n_{L0}^2 + (n_{L0}^2 - 1)r^2/R_C^2$ gradient described in Section 2.2, and Figures 11-12 incorporate a lower

peak laser power, i.e., ~ 0.1 MW (in order to remain below the nonlinear focusing power of As_2S_3 for frequency doubled-light). These figures (Fig. 11-12) also incorporate a (smooth) radial dip in the refractive linear index outside of a 500 μm radius which enables the beam to maintain its spot size over many Rayleigh lengths. Figures 8 and 10 are simulated according to the standard one-dimensional Nonlinear Schrodinger Equation with second order dispersion. Figures 2-7, 9, and 11-12 are simulated according to the BTUL code, i.e. Eq. (6), although Figure 9 is a 1D simulation (k_z becomes k, and the k_x and k_y arguments are ignored). For Figures 2-7 and 11-12, the backward-propagating field and backward-propagating polarization have been neglected; these simulations are unidirectional, and the nonlinear polarization term is the standard Kerr term, i.e. Eq. (5a). For Figure 9, which is bi-directional, the full polarization is calculated according to the two lined equations in Section 7.1 of the Supplement.

Our 3D simulations reproduce the spectrums in Ref. [5] in the 1D limit, i.e., $R_0 \rightarrow \infty$. However, when transverse effects are incorporated, self-focusing limits the propagation distance, thus reducing the degree of spectral broadening. We terminate the propagation when the on-axis intensity reaches roughly the breakdown intensity (~ 1 GW/cm^2). When an initially diverging beam with the parameters in Table 1 propagates in GaAs and self focuses until the intensity nears the breakdown threshold, a spectrum of $9 - 10$ μm can be achieved, see Fig. 2a, 3a. To obtain an $8 - 13$ μm spectral bandwidth requires a line spacing of $\Delta\lambda/\lambda \sim 0.04$, see Fig. 2b, 3b. Spectra presented here are spatially averaged, unless otherwise specified.

The spectrum obtained for a number of input conditions is shown in Fig. 3. The degree of spectral broadening in the long-wavelength regime is maximized for $\Delta\lambda/\lambda_0 = 0.04$. For large line separations the fractional bandwidth $\delta\omega/\omega_0$ is no longer proportional to $\Delta\lambda/\lambda_0$ due

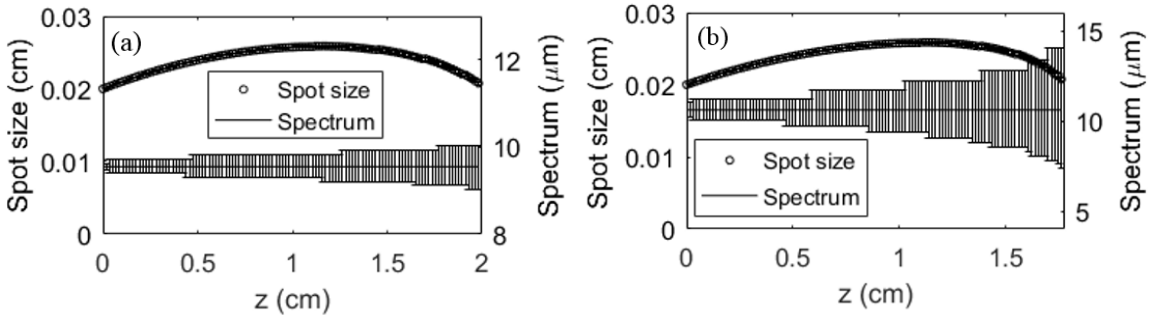

Figure 2: Self-focusing and spectral broadening of a beat wave propagating in GaAs, for the parameters of Table 1. The initial laser line separation is, respectively, (a) $\Delta\lambda/\lambda_0 = 0.01$, (b) $\Delta\lambda/\lambda_0 = 0.04$. In the latter case, the wavelength 10.6 μm has been used. The spot-size is determined by fitting the transverse laser profile to a Gaussian profile. The spectrum is defined here as the range over which there are individual frequency components containing at least 0.005% of the laser beam's total power, see Fig. 3.

to phase mismatch. In the normal dispersion regime ($\partial^2(\omega n(\omega))/\partial\omega^2 < 0$), e.g., $\lambda < 7$ μm for GaAs, dispersion effects broaden the laser pulse duration, thus reducing the rate of spectral broadening. Spectral broadening in the normal dispersion regime is shown in Fig. 3c.

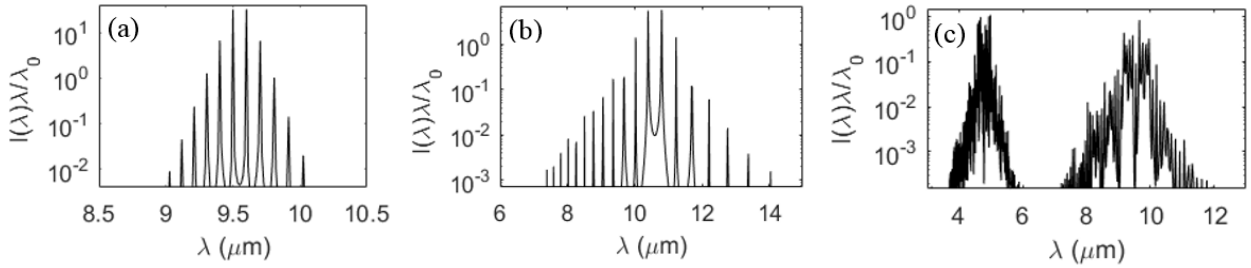

Figure 3: Spectrum of a beat wave propagating in GaAs, for the parameters in Table 1. The spectrum is shown at a distance when the on-axis intensity nears the breakdown threshold. The input laser line separation is, respectively, (a) $\Delta\lambda/\lambda_0 = 0.01$, (b) $\Delta\lambda/\lambda_0 = 0.04$, (c) $\Delta\lambda/\lambda_0 = 0.08$. These lines are comprised of 8 individual lines in the range from 9.15 μm – 9.95 μm , together with eight lines in the range 4.575 μm – 4.975 μm, where each line contains 0.08 MW.

The propagation distance can be extended by operating near the nonlinear focusing power P_K . Propagation over several Rayleigh lengths ($Z_R = 4$ cm) is shown in Fig. 4. The resulting spectral broadening is in good agreement with Eq. (11), see Fig. 5. The spectral broadening in this case is larger than that obtained when operating above the nonlinear focusing power

(see Fig. 2a, 3a) because the pulse propagates longer distances before radial collapse.

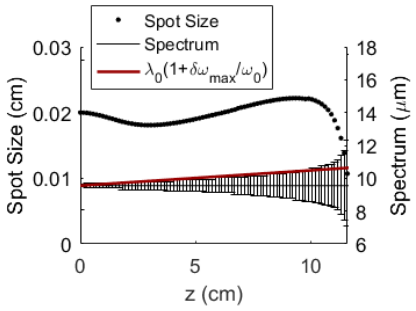

Figure 4: Self-focusing and spectral broadening of a beat wave near the focusing power in GaAs. The peak power here is P $=$ 0.93 P_K .

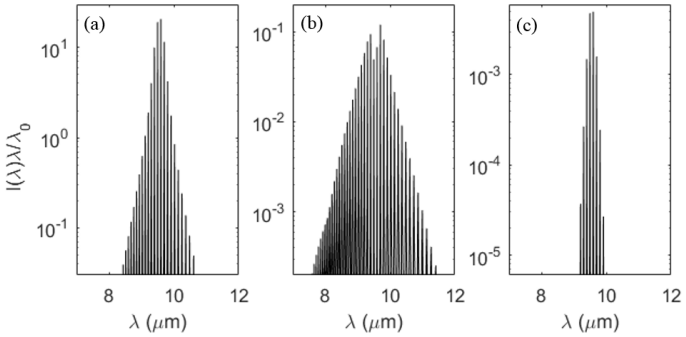

Figure 5: The total power spectrum, at z = 11.2 cm, is shown in (a) for a beat wave near the focusing power. The spectrum (b) on-axis and (c) at the spot size R_0 are shown for comparison. The spectrum is broader along the axis because of the higher intensity on axis.

3.2 Spectral Broadening in an Index Tapered Medium

An alternative way to overcome the limitations due to self-focusing when P > P_K is to operate in a GaAs rod with a radially-graded refractive index. In the following example, a graded-index rod in which the refractive index increases as a function of r^2 is used to defocus the beam, thereby mitigating the nonlinear self-focusing and extending the propagation distance, see Fig. 6. A supercontinuum which extends beyond 5 – 14 μm can be obtained. We note

that each pulse is compressed tenfold, see Discussion. The spectral broadening in a graded GaAs rod exceeds that in a uniform GaAs rod, see Fig. 7 and Fig. 3b.

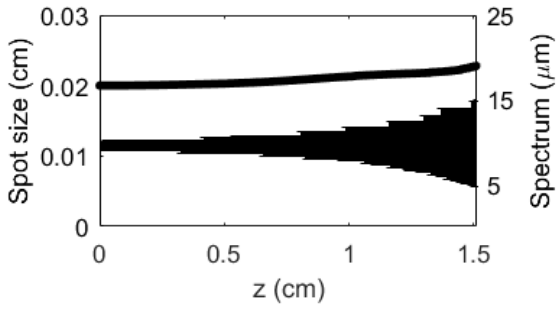

Figure 6: Self-focusing and spectral broadening of a Gaussian-profile laser beat wave propagating through a GaAs waveguide with a graded index. The laser line separation is $\Delta\lambda/\lambda_0 = 0.04$, and the peak power is given by $\mathrm{P/P}_K = 5$.

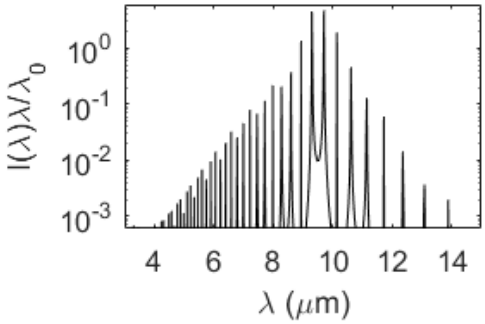

Figure 7: Power spectrum for $\Delta\lambda/\lambda_0 = 0.04$ after propagating 1.5 cm in a GaAs rod with a graded index characterized by $R_C = 70\ R_0$, see Fig. 6

3.3 Effect of Laser Phase Noise on Spectral Broadening

Given that high power CO_2 lasers can be 'noisy', i.e., have a substantial laser line width, see Ref. [13], the effect of laser noise on spectral broadening is an important consideration for enhancing spectral broadening in a dispersive, nonlinear medium.

We model the phase noise of the CO_2 laser according to a phase diffusion model [14]. Laser noise effects are typically dominated by phase noise and not intensity noise [15]. In

the following, intensity laser noise is neglected. In a dispersive medium the phase noise can result in intensity fluctuations [16-17]. In addition, if the medium has a Kerr nonlinearity the fluctuations lead to additional spectral broadening via self–phase modulation and other nonlinear processes, see Fig. 8.

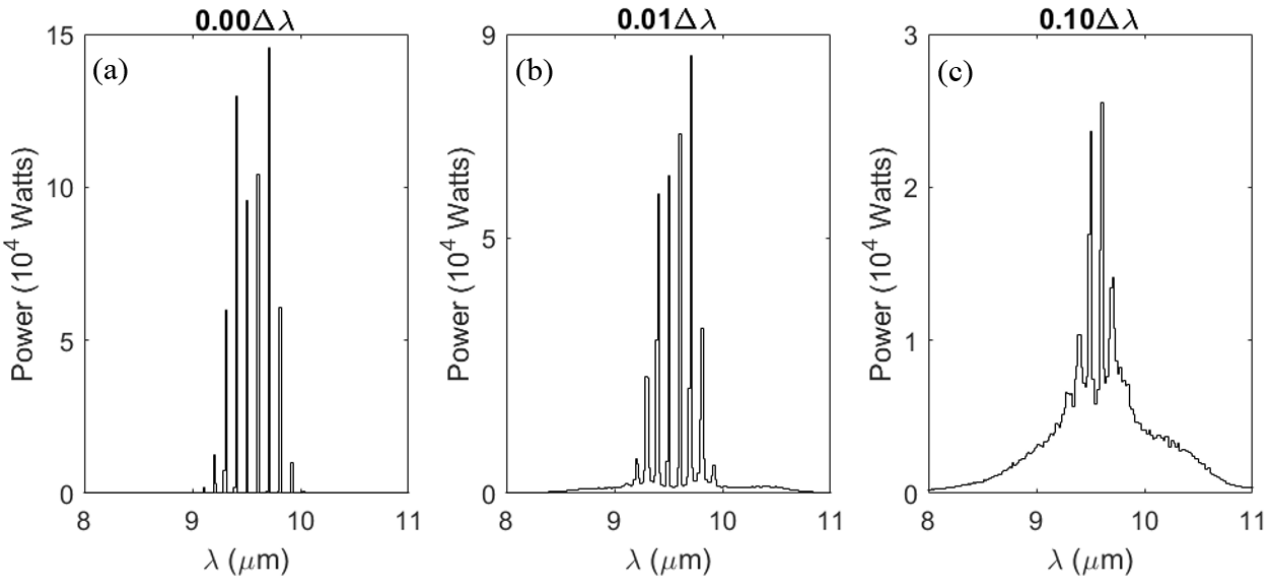

Figure 8: Power per wavelength-regime, given a varying laser linewidth due to phase noise. The total power in spectrum (a), (b), and (c) is the same. The spectrum is shown after propagating 2 cm in GaAs. Initially the CO_2 radiation consisted of two lines each with linewidth (a) $0.00\Delta\lambda$ (no noise) (b) $0.01\Delta\lambda$ (c) $0.10\Delta\lambda$ due to phase noise. The initial laser line separation is $\Delta\lambda/\lambda_0 = 0.01$. In frequency space this corresponds to (a) 0 GHz (no noise) (b) 3 GHz (c) 30 GHz.

The area under the curves in each plot in Fig. 8 is equal. In Fig. 8a, 1 MW of power is contained between the wavelengths 9.0 and 10.1 μm. In Fig. 8b, the same amount of power is contained between 8.0 and 11 μm. Finally in Fig. 8c, 1 MW of power is contained between 7.7 to 11.5 μm. Note that in Fig. 8c the spectrum approaches a continuum.

For a high-power CO_2 laser with laser linewidth $\sim$ 500 MHz, phase noise does not significantly affect the laser propagation, given the parameters in Table 1. The same is true for intensity noise, which can be incorporated by instead modeling the laser noise as a collection

of $N \gg 1$ single-frequency, uncorrelated emitters distributed according to the spectral line shape, see Ref. [18]. Increasing the laser linewidth, however, can significantly enhance the spectral broadening, see Fig. 8.

We note that when two substantial frequency lines amplify a third line from the background via four wave mixing (FWM), the total amplification $\exp(g\ z)$ (where g is the FWM gain) is so large that the magnitude and structure of the background noise have little effect on the resulting spectral bandwidth. In the case of white noise distributed from $\omega_0/2$ to $2\omega_0$, for example, this can be true for noise field magnitudes up to $|\delta E/E| \sim 1/10$.

3.4 Enhancement of Spectral Broadening via Coupling to a Backward-Propagating, Reflected Wave

A backward-propagating wave nonlinearly induces temporal fluctuations in the refractive index of the medium. These fluctuations induce a phase shift in the forward-propagating wave which can result in spectral broadening.

The BTUL bidirectional simulations are in agreement with the dispersion relation in Eq. (12) for the modulation instability, and predict that coupling to a backward-propagating, reflective wave can enhance the spectral broadening over substantial propagation distances specifically in the anomalous dispersion regime of a nonlinear medium, see Fig. 9.

We note that the backwards-propagating wave cannot directly induce new frequencies in a forward-propagating wave via four wave mixing due to a phase mismatch.

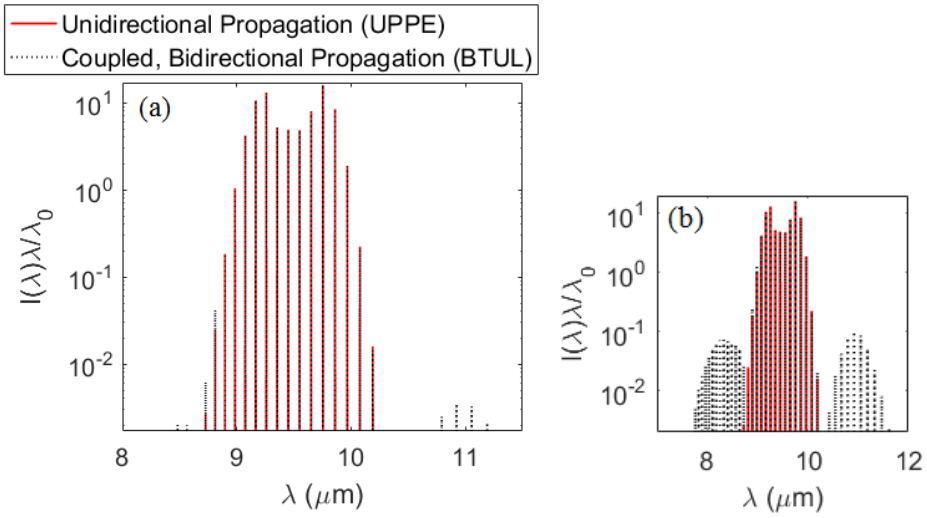

Figure 9: The power spectrum is shown at $z = 3$ cm for a forward-propagating beat-wave in GaAs with the parameters in Table 1, with coupling to a backward-propagation reflected wave. This simulation has been carried out in 1D for an initial laser line separation of $\Delta\lambda/\lambda_0 = 0.02$ and demonstrates the usefulness of BTUL's bi-directional capability as well as the ability of a backward-propagating reflected wave to enhance spectral broadening in the anomalous dispersion regime of a nonlinear medium. (a) The black dotted curve represents propagation given 29% reflectivity at the end of the medium (i.e., at $z = 3$ cm), corresponding to reflection off a GaAs - Air boundary. The red, solid curve corresponds to 0% reflectivity, i.e., unidirectional propagation. (b) The black dotted curve represents propagation given 100% reflectivity at the end of the medium.

3.5 Second-Harmonic Spectral Broadening in As_2S_3 Fiber

Chalcogenide (As_2S_3) is a promising material for spectral broadening in the long-wave IR regime. The benefits are (i) the significant nonlinear refractive index (∼1/6 that of GaAs), (ii) the long propagation distances (∼8 m) attainable via low-loss As_2S_3 optical fibers [19], see Eq. (11), and (iii) the small group velocity dispersion coefficient in the vicinity of its zero dispersion wavelength at 4.8 μm. These benefits are apparent in 1D simulations which incorporate the full dispersion relation of GaAs and As_2S_3, see Fig. 10. The fractional bandwidth $\delta\omega/\omega_0$ as a function of propagation distance is estimated here via the third moment in frequency space $\mu_3(z) = \langle(\omega-\omega_0)^3\rangle^{1/3} = \left(\int P(\omega,z)\mathrm{d}\omega\right)^{-1}\left(\int(\omega-\omega_0)^3 P(\omega,z)\mathrm{d}\omega\right)^{1/3}$, where $\omega_0 = 2\pi c/\lambda_0$ is the laser frequency and $P(\omega,z)$ is the power spectrum as a function of the propagation distance z of a CO_2 laser-beat wave through GaAs, As_2S_3, respectively.

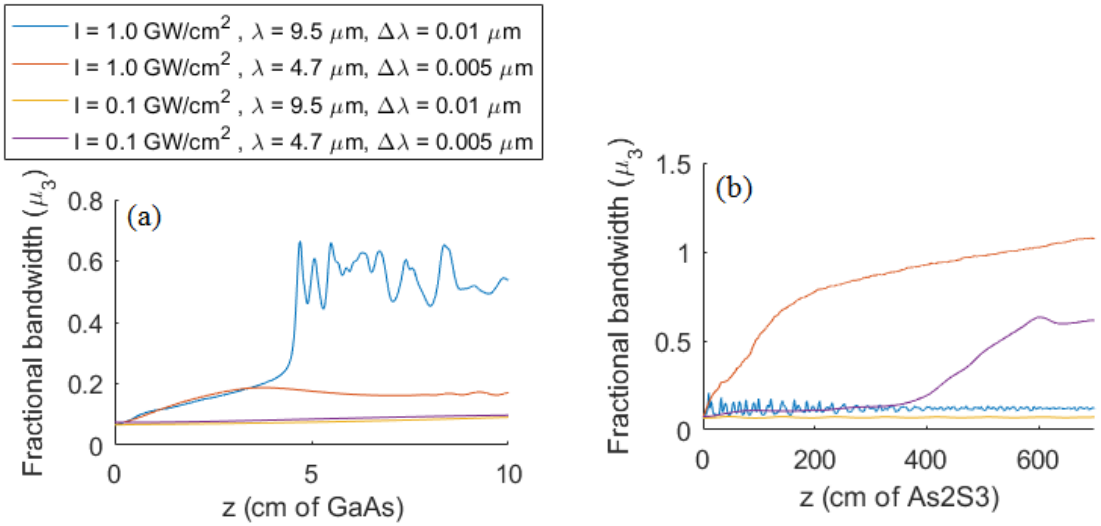

Figure 10: 1D simulation of CO_2 laser beat-wave propagating through (a) GaAs (b) As_2S_3 at various intensities and wavelengths. The fractional bandwidth is estimated here as the third moment in frequency space, i.e. $\mu_3(z) = \left(\int P(\omega,z)\mathrm{d}\omega\right)^{-1}\left(\int(\omega-\omega_0)^3 P(\omega,z)\mathrm{d}\omega\right)^{1/3}$.

To simulate laser propagation through a chalcogenide (As_2S_3) fiber, we represent the

cladding as a $\Delta n_L = 1.0$ dip in the refractive index with a radius 2.5 R_0 with its ramp occurring over a transverse distance of 30 λ_0. The divergence term of the field is incorporated, see Eq. (2). We see that a 4 – 6 μm bandwidth can be achieved via the propagation of a multi-line frequency-doubled CO_2 beat-wave through a chalcogenide fiber at just one tenth of the intensity and power given in Table 1, see Fig. 11 – 12.

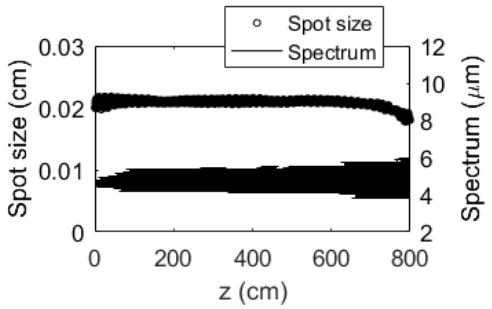

Figure 11: Optical guiding, self-focusing, and spectral broadening of a Gaussian-profile frequency-doubled CO_2 beat-wave with 200 μm initial spot size, laser wavelength $\lambda_0 = 4.7$ μm, and laser line separation $\Delta\lambda/\lambda_0 = 0.005$ propagating through an As_2S_3 fiber. Although the laser operates below the nonlinear focusing power $P_K \propto \lambda^2$, extreme spectral broadening yields high frequency components which are indeed above their respective nonlinear focusing power.

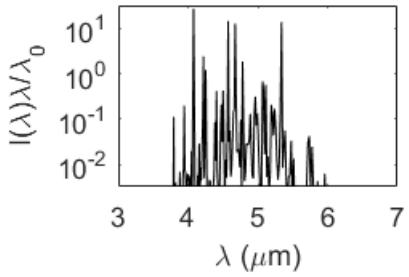

Figure 12: Power spectrum for $\Delta\lambda/\lambda_0 = 0.005$, where $\lambda_0 = 4.7$ μm , after propagating 8 meters in an As_2S_3 fiber, see Fig. 10.

4 Discussion

Carbon Dioxide lasers have tunable lines in the 9 – 11 μm range and can be frequency doubled. Transversely excited atmospheric (TEA) CO_2 lasers can provide average output powers of tens of kilowatts together with repetition rates from kHz to as high as 100 kHz, and have long operating lifetimes in excess of 10^4 hours [20]. Commercially available TEA CO_2 lasers are compact and relatively low cost per watt. They can have average power levels in the multi tens of kW range and operating efficiencies as high as 30%.

4.1 Raman Scattering

Raman amplification of input noise by a CO_2 laser will impede the spectral broadening in a GaAs waveguide at propagation distances beyond a characteristic Raman amplification length [21]. For a CO_2 laser of average power $P = 2.5\ P_K$ and spot size $R_0 = 0.02$ cm we find that the characteristic Raman amplification length is $L_{CR} \approx 3$ cm [22].

In the case of second-harmonic spectral broadening in a chalcogenide fiber, Brillouin scattering may play an important role, depending on the laser bandwidth and pulse length. Further studies are required.

The energy backscattered via other nonlinear and linear processes has been neglected here in Part II, given the homogeneity of GaAs crystals, the availability of custom anti-reflection coatings, and the relatively modest peak powers.

4.2 Laser Damage Threshold

Laser damage to the GaAs and the optics is an important consideration in the applications of ultra-broadband IR radiation. A 3 – 8 MW/mm^2 intensity threshold was measured at the Hirst Research Centre for propagation through GaAs of a 50 mJ CO_2 laser pulse with a third of the pulse energy in a 60 ns pulse width [23]. In the thermal damage regime, the intensity threshold is approximately independent of the pulse duration and inversely proportional to the spot size [24]. The parameters of Table 1 indicate an intensity threshold of 0.4 – 1.5 GW/cm^2. This is consistent with the finding in Ref. [2] that 0.7 GW/cm^2 is safely below the intensity threshold. The simulations here in Part II remain below 1 GW/cm^2 on the timescale of multiple micropulses (¿10 ps), and each micropulse is restricted to 10 GW/cm^2.

Surface damage sets an energy density threshold, thereby limiting the allowed pulse duration. The parameters given in Ref. [5] exceed this damage threshold for the proposed 200 ns CO_2 TEA laser pulse, which has an energy density of 200 J/cm^2 and higher on-axis. An energy density limit of 1 – 2 J/cm^2 in the optics and coating was reported in Ref. [3]. For high average power applications, it may be useful to experiment with higher energy densities using an uncoated GaAs crystal and Cu/Ni/Au mirrors, see Fig. 9 and Ref. [25].

5 Conclusion

We have developed a three-dimensional ultra-broadband laser propagation code (BTUL) which can treat coupled forward and backward propagating waves in a nonlinear, dispersive medium. We have also demonstrated that 3D effects play an important role in the spectral broadening

process. One dimensional models of spectral broadening can overestimate the degree of broadening by almost an order of magnitude. Our 3D simulations show that when operating near or above the nonlinear focusing power, the fractional line width separation of $\Delta\lambda/\lambda_0 \approx 0.04$ leads to substantial broadening in GaAs. This linewidth separation appears to be near optimal given the parameter range considered. We have also demonstrated that the use of a graded-index or cladding around the nonlinear medium can extend the propagation range and therefore the degree of spectral broadening. The beat-wave formed by two CO_2 lines can generate a spectrum extending beyond 5 – 14 μm via propagation through a graded-index GaAs rod, and the beat-wave formed by two frequency-doubled CO_2 lines can generate a spectrum of 4 – 6 μm via propagation through a As2S3 fiber. In addition, we have shown enhancement of spectral broadening via coupling to a backward-propagating reflected wave in the anomalous dispersion regime of a nonlinear medium. Finally, we have shown that laser phase noise in a dispersive medium can be a significant contributor to spectral broadening.

6 References

[1] Corkum, P.B., Ho, P.P., Alfano, R.R. and Manassah, J.T., 1985. Generation of infrared supercontinuum covering 3–14 μm in dielectrics and semiconductors. Optics letters, 10(12), pp.624-626.

[2] Pigeon, J. J., S. Ya Tochitsky, C. Gong, and C. Joshi. "Supercontinuum generation from 2 to 20 μm in GaAs pumped by picosecond CO 2 laser pulses." Optics letters 39, no. 11 (2014): 3246-3249.

[3] Pigeon, J.J., Tochitsky, S.Y. and Joshi, C., 2015. High-power, mid-infrared, picosecond

pulses generated by compression of a CO 2 laser beat-wave in GaAs. Optics letters, 40(24), pp.5730-5733.

[4] Pigeon, J., Tochitsky, S. and Joshi, C., 2016, March. Generation of broadband 10 μm pulses using four-wave mixing compression in GaAs. In Mid-Infrared Coherent Sources (pp. MT2C-7). Optical Society of America.

[5] Kapetanakos, C.A., Hafizi, B., Milchberg, H.M., Sprangle, P., Hubbard, R.F. and Ting, A., 1999. Generation of high-average-power ultrabroad-band infrared pulses. IEEE journal of quantum electronics, 35(4), pp.565-576.

[6] Kapetanakos, C.A., Hafizi, B., Sprangle, P., Hubbard, R.F. and Ting, A., 2001. Progress in the development of a high average power ultra-broadband infrared radiation source. IEEE journal of quantum electronics, 37(5), pp.641-652

[7] Dudley, J.M., Genty, G. and Coen, S., 2006. Supercontinuum generation in photonic crystal fiber. Reviews of modern physics, 78(4), p.1135.

[8] Kolesik, M., Moloney, J.V. and Mlejnek, M., 2002. Unidirectional optical pulse propagation equation. Physical review letters, 89(28), p.283902.

[9] Kolesik, M. and Moloney, J.V., 2004. Nonlinear optical pulse propagation simulation: From Maxwell's to unidirectional equations. Physical Review E, 70(3), p.036604.

[10] Andreasen, J., and M. Kolesik. "Nonlinear propagation of light in structured media: Generalized unidirectional pulse propagation equations." Physical Review E 86, no. 3 (2012): 036706.

[11] Esarey, E., Sprangle, P., Krall, J. and Ting, A., 1997. Self-focusing and guiding of short laser pulses in ionizing gases and plasmas. IEEE Journal of Quantum Electronics, 33(11),

pp.1879-1914.

[12] Sprangle, P., Penano, J.R. and Hafizi, B., 2002. Propagation of intense short laser pulses in the atmosphere. Physical Review E, 66(4), p.046418.

[13] Duarte, F.J., 1986. Variable linewidth high-power TEA CO2 laser." Applied optics 24(1), pp. 34-37.

[14] Frosz, M.H., 2010. Validation of input-noise model for simulations of supercontinuum generation and rogue waves. Optics express, 18(14), pp.14778-14787.

[15] Schubert, M., K-E. Susse, W. Vogel, and D-G. Welsch. "Influence of fluctuations of a laser pump on the intensity correlation of resonance fluorescence radiation." Optical and Quantum Electronics 12, no. 1 (1980): 65-76.

[16] Marshall, W.K., Crosignani, B. and Yariv, A., 2000. Laser phase noise to intensity noise conversion by lowest-order group-velocity dispersion in optical fiber: exact theory. Optics letters, 25(3), pp.165-167.

[17] Isaacs, J. Sprangle, P., "The Effect of Laser Noise on the Propagation of Laser Radiation in Dispersive and Nonlinear Media," Proc. SPIE, Submitted.

[18] Nelson, W., Sprangle, P. and Davis, C.C., 2016. Atmospheric propagation and combining of high-power lasers. Applied optics, 55(7), pp.1757-1764.

[19] "Chalcogenide Glass Fibers." IRFlex Corporation. Accessed March 19, 2018. https://www.irflex.com/products/irf-s-series/.

[20] A. J. DeMaria and T. V. Hennessey, SPIE Professional Magazine, 50th Anniversary of Laser Devices (2010).

[21] Agrawal, G. (2013). Nonlinear fiber optics. 5th ed. Academic Press.

[22] WD Johnston, J.R. and Kaminow, I.P., 1969. Contributions to optical nonlinearity in GaAs as determined from Raman scattering efficiencies. Physical Review, 188(3), p.1209.

[23] Wood, R.M., Sharma, S.K. and Waite, P., 1983, June. Review of laser induced damage thresholds. In The Max Born Centenary Conference (pp. 84-87). International Society for Optics and Photonics.

[24] Wood, R.M., 2003. Laser-induced damage of optical materials. CRC Press.

[25] Cu/Ni/Au Mirrors. Retrieved January 1, 2017, from http://www.haaslti.com/copper-mirror-laser.html

7 Supplement

7.1 Supplement: Evaluation of Nonlinear Polarization Term

When a forward propagating field is coupled to a non-perturbative backward propagating field, Eq. (4) must be generalized as follows: The nonlinear polarization field is given by

$$\tilde{P}_{NL}^{\pm}(k_x, k_y, z, \omega) = \varepsilon_0 \chi_{NL} \iiint \exp(i\omega t - ik_x x - ik_y y) \mathrm{d}t \mathrm{d}x \mathrm{d}y \times$$
$$\left(\left(E^{\pm}(\mathbf{r}, t)\right)^3 + 3 \left\{ \left(E^{+}(\mathbf{r}, t)\right)^2 E^{-}(\mathbf{r}, t) + \left(E^{-}(\mathbf{r}, t)\right)^2 E^{+}(\mathbf{r}, t) \right\}^{\pm} \right)$$

Evaluation of the right-hand term requires knowledge of the directionality of each component of $(E(\mathbf{r}, t))^3$. To directly determine the directionality would require appending the

variable $k_z = \pm\left(k^2(\omega) - k_x^2 - k_y^2\right)^{1/2}$ to the (k_x, k_y, ω) vector space. This is inefficient and generally exceeds the computational memory limit. Rather, it is appropriate to divide the forward and backward going field into frequency regimes as a means of resolving directionality. For example, in the case where $\delta\omega/\omega_0 < 2/3$, we can divide the forward and backward going field into two frequency regimes, i.e., $\omega > 0$, $\omega < 0$. Denoting these regimes by a subscript, i.e., $E^{\pm}_{\omega<0}$, $E^{\pm}_{\omega>0}$, the nonlinear polarization field $\tilde{P}^{\pm}_{NL}$ can be written as:

$$\tilde{P}^{\pm}_{NL}(k_x, k_y, z, \omega) = \varepsilon_0 \chi_{NL} \iiint \exp(i\omega t - ik_x x - ik_y y)\mathrm{d}t\mathrm{d}x\mathrm{d}y \times \left(\begin{array}{l} \left(E^{\pm}(\mathbf{r}, t)\right)^3 + 6E^{\mp}_{\omega>0}(\mathbf{r}, t)E^{\mp}_{\omega<0}(\mathbf{r}, t)E^{\pm}(\mathbf{r}, t) + \\ \\ 3\left(\left(E^{\pm}_{\omega>0}(\mathbf{r}, t)\right)^2 + \left(E^{\pm}_{\omega<0}(\mathbf{r}, t)\right)^2\right)E^{\mp}(\mathbf{r}, t) \end{array} \right)$$

To derive this relation, each field component $C_{\omega',k'} \exp(ik'z - i\omega' t)$ is represented as the vector (ω', k') in $\omega - k$ space, where the field is general and can decomposed as $E(\mathrm{r}, t) = \iint C_{\omega',k'} \exp(ik'z - i\omega' t)\mathrm{d}\omega'\mathrm{d}k'$. For example, a field propagating in the forward direction contains components in the $(+,+)$ and/or $(-,-)$ quadrant of $\omega - k$ space. Each component of $(E(\mathbf{r}, t))^3$ represents the combination of 3 fields, i.e. the sum of 3 vectors in $\omega - k$ space.

7.2 Supplement: Numerical Techniques

With the exception of Section 3.4, the simulations only involve unidirectional propagation; BTUL then reduces to a 3D UPPE which takes the form of an ODE. It is solved in 3D Fourier space via iterative determination of the field's slope along the longitudinal axis. The nonlinear polarization density at each step along the longitudinal axis is calculated in the time domain.

Negative frequency components are included in the analysis, and the sign of k_z in Section 2.1 is defined accordingly, i.e., $k_z(k_x, k_y, z, -\omega) = -k_z(k_x, k_y, z, \omega)$ for $\omega > 0$.

Regarding the additional terms which are absent in a traditional UPPE: The divergence term can be numerically integrated beside the nonlinear polarization density term. In the case of a spatially varying refractive index, the additional term below Eq.(6) is incorporated at each step Δz in spatial coordinates via the operator $\exp\left(i\ \delta k^2(x, y, z, \omega)E(x, y, z, \omega)\ \Delta z\ /\ 2k_0\right)$.

In all simulations with the exception of Section 3.3, periodic temporal boundary conditions are employed. Hence, a pulse duration has been specified in Table 2 which well exceeds the dispersion-induced walk-off time.

For bi-directional propagation, in summary - iteration from forward propagation to backward propagation to forward propagation etc. converges to a stable solution, which represents the middle of a long pulse which contains within it periodic behavior. For each iteration, the electric field at each point along the propagation axis is stored in an array in order to be incorporated into the nonlinear polarization expression given in the Supplement.

With the exception of Fig. 8-10, all simulations are carried out in three spatial dimensions. To analyze the transverse beam profile of the propagating beam, we define an 'effective spot size' $R_{\mathrm{Eff}}(z)$ and 'effective on-axis intensity' $\mathrm{I}_{\mathrm{Eff}}(z)$ as the parameters determined by fitting the transverse beam profile $I(x, y)$ to a Gaussian surface $G(x, y)$ given by $G(x, y) = \mathrm{I}_{\mathrm{Eff}} \exp\left(-2x^2/R_{\mathrm{x}}^2 - 2y^2/R_{\mathrm{y}}^2\right)$, $R_{\mathrm{Eff}} = (R_{\mathrm{x}}^2 + R_{\mathrm{y}}^2)^{1/2}$. Consistency between BTUL and the 3D Nonlinear Schrodinger Equation (NLSE) has been benchmarked.

Guard bands are placed in transverse space and in transverse spatial frequency space. The guard bands absorb all energy beyond some spatial bound and spatial frequency threshold,

thereby avoiding aliasing across the periodic boundary imposed by the Fast Fourier Transform operation. Grid resolution requirements in both vector spaces are also imposed. The dotted line in Fig. 13a indicates the resolution limit $R_{\mathrm{Eff}}(z) = 3\Delta x_{\mathrm{grid}}$ below which the beam may be insufficiently resolved in transverse space, where Δx_{grid} denotes the transverse distance between grid points.

As a laser beam self-focuses towards collapse, transverse spatial frequencies above a specified threshold will be generated and then absorbed by the guard bands in order to avoid aliasing. When significant guard band absorption occurs, the BTUL code terminates the propagation in order to avoid nonphysical results associated with the exclusion of sharply converging field components.

As a simple benchmark, BTUL is used to reproduce the power law for a monochromatic, perfect Gaussian beam , see Fig. 13a and 13b, where the self-focusing distance is defined as the collapse distance, i.e., $\lim_{z\to z_{\mathrm{SF}}} R_{\mathrm{Eff}}(z)/R_0 = 0$. The extrapolated collapse distance is compared, respectively, to the numerical result $z_{\mathrm{SF}}(\mathrm{P}, \mathrm{P_K}, R_0)$ [9].

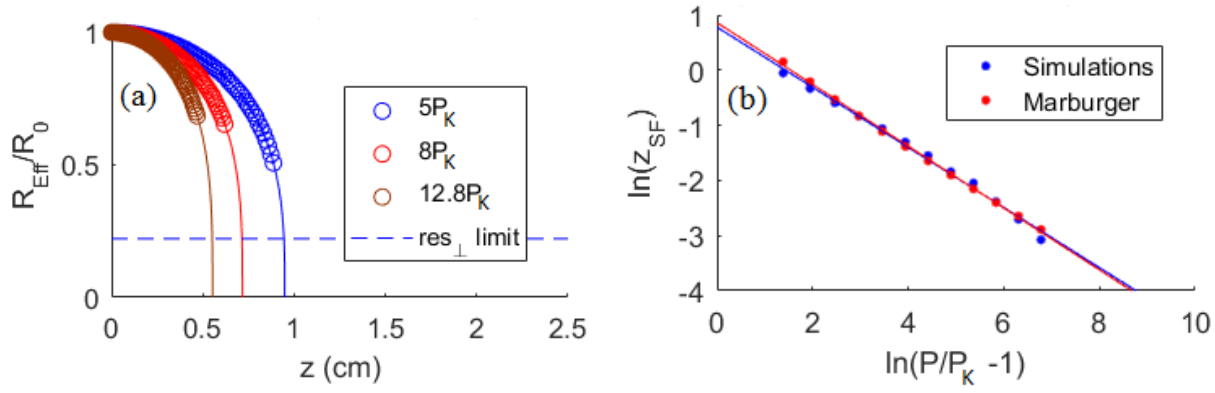

Figure 13: (a) The effective spot size of a Gaussian-profile, monochromatic laser beam of initial spot size $R_0 = 200$ μm is plotted as a function of propagation distance through GaAs for various input powers 'P' which are above the nonlinear focusing power, i.e. $P > P_K = 2\pi c^2/(\omega_0^2 n_0 n_2) = 0.26$ MW. The collapse distance is extrapolated and (b) plotted as a function of input power in order to show consistency with an approximate numerical formula [9] for the collapse distance.

Part III

Spectral Broadening of the NIKE KrF Laser in a Negative Nonlinear Index Medium

In inertial confinement (ICF) experiments at the NIKE [1] laser facility, the high-power krypton fluoride (KrF) laser output beams propagate through long (∼75m) air paths to achieve angular multiplexing. This is required because the KrF medium does not store energy for a sufficiently long time. Recent experiments and simulations have shown that, via stimulated rotational Raman scattering (SRRS), this propagation can spectrally broaden the laser beam well beyond the ∼1 THz laser linewidth normally achieved by the induced spatial incoherence (ISI) technique used in NIKE [2]. These enhanced bandwidths may be enough to suppress the laser-plasma instabilities which limit the maximum intensity that can be incident on the ICF

target. We investigate an alternative technique that achieves spectral broadening by self-phase modulation in Xe gas, which has a large, negative nonlinear refractive index $\sim$ 248 nm [3], and thus completely avoids transverse filamentation issues. The collective, nonlinear atomic response to the chaotic, non-steady state ISI light is modeled using a two-photon vector model. The effect of near-resonant behavior on the spectral broadening is also studied.

1 Introduction

A primary challenge in inertial confinement fusion is the growth of hydrodynamic instabilities and laser plasma instabilities (LPI) [4]. Increasing the laser spectral bandwidth can be an effective way of reducing the growth rates of LPI instabilities [1]. Recent experiments on the NIKE KrF laser, which uses a 75 m propagation bay for beam multiplexing, have shown that stimulated rotational Raman scattering (SRRS) in the air paths can spectrally broaden the bandwidth of the chaotic, incoherent light well beyond the $\sim$ 1 THz normally allowed by NIKE's induced spatial incoherence (ISI) technique. While SRRS is small in normal NIKE operation at moderate beam intensities ($\sim$ 50 MW/cm^2), these experiments generated significant SRRS by imposing a $\sim$ 150 MW/cm^2, 400 ps spike on the pulse and folding the beam to lengthen the optical air path. The amount of spectral broadening that was achieved, however, was limited to several THz. Alternatively, to propagate in an inert gas requires a large nonlinear refractive index $n_2 \sim 60 \times 10^{-19}$cm^2/W - five times that of air - for comparable spectral broadening. Though this would mean self-filamentation for a Gaussian beam (where the nonlinear focusing power at 248nm in air is 100 MW), the important parameter for ISI light is the power within a single coherence zone; for a 75 times diffraction limited beam, the

nonlinear focusing power in air becomes $\sim$ 500 GW.

For linearly polarized light, there exists a two-photon resonance in atomic xenon (Xe) at 249.6 nm which has been discussed in the literature [3,5]. As a result of this resonance, Xe has a large, negative nonlinear index n_2 at the 248.4nm KrF laser wavelength whose doubled frequency lies only 11.9 THz above the resonance, see Fig. 14-15. Hence, propagation through Xe gas has the potential to substantially increase the spectral bandwidth of the KrF laser without the problem of self-filamentation, which is a positive-n_2 effect. The negative nonlinear index near-resonance has been observed and accurately calculated from known Xe electric dipole matrix elements for narrowband KrF light operating under steady-state conditions [3,6].

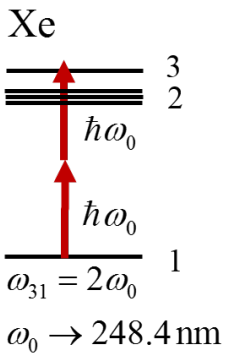

Figure 14: The nonlinear optical response of Xe near its two-photon $5p^6 \rightarrow 6p[1/2]_0$ resonance is that of a three-level system with multiple intermediate states $|2\rangle$, and allowed electronic transitions from $|1\rangle \rightarrow |2\rangle$ and $|2\rangle \rightarrow |3\rangle$.

At the NIKE facility, however, the KrF laser uses incoherent beam smoothing techniques that produce chaotic variations on a ps timescale. The resulting multi THz spectral bandwidths of interest can thus include frequencies that are much closer to the two-photon resonance than the 11.9 THz detuning of the narrowband KrF light. As a result, the nonlinear Kerr response can experience time delays and the upper level may become partially populated

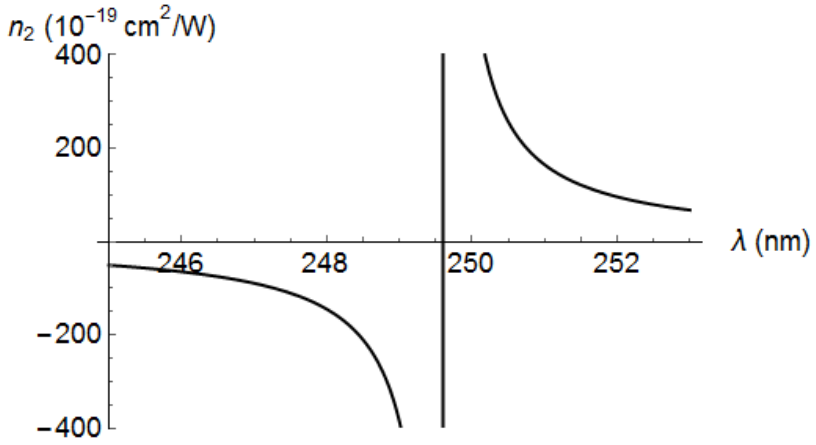

Figure 15: Wavelength-dependence of the nonlinear refractive index n2 of 200mbar Xe in the regime of the two-photon resonance. The curve is continuous but extends beyond the range shown here.

during the pulse.

We model the nonlinear response of Xe gas to chaotic non-steady-state, near-resonance light using a two-photon vector model. Although this model includes small collisional damping coefficients, they play a negligible role in spectral broadening at Xe pressures up to at least 200mbar. At 200mbar, nonlinear effects and linear attenuation due to the small (0.02%) dimerization of the Xe molecules are expected to be minimal, but further investigation is needed, see Ref. [3,15]. Earlier work on two-photon vector models can be found in Ref. [7-8].

Though the laser propagation in a nonlinear medium yields spectral broadening (which is useful for the reduction of hydrodynamic and laser plasma instabilities in inertial confinement fusion) the propagation also results in far-field broadening. The resulting degradation of the laser beam profile is studied.

A detailed overview of the NIKE laser facility and its KrF laser can be found in Ref. [1]. The NIKE laser facility uses echelon-free induced spatial incoherence (ISI) to produce a laser beam that is spatially and temporally incoherent [9-10]. The beam's speckle fluctua-

tions occur over rapid (picosecond) timescales such that they average out over hydrodynamic timescales to yield a spatially and temporally uniform illumination. This, in turn, minimizes the hydrodynamic instabilities that would otherwise be strongly seeded by laser beam spatial nonuniformities.

In Section 2, we present the Nonlinear Schrodinger Equation that is used to model laser propagation through a nonlinear medium, discuss how to model the directed spatially and temporally incoherent KrF radiation, derive a model for the nonlinear response of the Xe gas, and describe the numerical techniques. In Section 3, we present simulation results. In Section 4, we discuss the results and propose a new direction for the inertial confinement fusion experiments at the NIKE laser facility. In Section 5, we summarize our results.

2 Model

2.1 Laser Pulse Propagation - Generalized Nonlinear Schrodinger Equation

In the absence of free charges, the electric field is given by the wave equation with a nonlinear source term, i.e.

$$\nabla^2 E(\mathbf{r},t) = (\partial/\partial t)^2 E(\mathbf{r},t)/c^2 + \mu_0(\partial/\partial t)^2 \left(P_L(\mathbf{r},t) + P_{NL}(\mathbf{r},t)\right),$$

where $P_L(\mathbf{r},t)$ and $P_{NL}(\mathbf{r},t)$ are respectively the linear and nonlinear polarization of the propagation medium. The electric field is taken to be linearly polarized along the x-axis, and the

divergence term has been neglected since the beam's spatial fluctuations occur over distances much larger than the wavelength.

Because (a) the nonlinear changes in the refractive index are small relative to the linear changes in the refractive index and (b) the KrF laser's fractional bandwidth $\Delta\omega/\omega_0 \ll 1$, we can make a slowly varying envelope approximation and express the wave equation as a three-dimensional generalization of the Nonlinear Schrodinger Equation (NLSE) [11]. The envelope equation is given by

$$\begin{aligned}(\partial/\partial\eta)E_p(\mathbf{r},\tau) =& i\nabla_\perp^2 E_p(\mathbf{r},\tau)/2k_0 + \left(-i\beta_2(\partial/\partial\tau)^2 E_p(\mathbf{r},\tau)/2 + ...\right) \\ &+ i\left(\omega_0^2/2\varepsilon_0 c^2 k_0\right)\left(1 + i(\partial/\partial\tau)/\omega_0\right)^2 P_{NL,p}(\mathbf{r},\tau)\ ,\end{aligned} \tag{1}$$

where $\eta = z$ and $\tau = t - z/\mathrm{v}$ are the longitudinal and temporal variables in a frame moving at the group velocity v, k_0 is the wavenumber at the carrier frequency $\omega_0 = 2\pi c/\lambda_0$, and β_2 is the group velocity dispersion coefficient at ω_0. The electric field is given by $E(\mathbf{r},t) = (1/2)E_p(\mathbf{r},t)\exp(ik_0 z - i\omega_0 t) + (1/2)E_p^*(\mathbf{r},t)\exp(-ik_0 z + i\omega_0 t)$, and the nonlinear polarization field (excluding higher harmonics) is given by

$P_{NL}(\mathbf{r},t) = (1/2)P_{NL,p}(\mathbf{r},t)\exp(ik_0 z - i\omega_0 t) + (1/2)P_{NL,p}^*(\mathbf{r},t)\exp(-ik_0 z + i\omega_0 t)$. The wave equation given in Eq. (1) can be solved numerically via the split-step method, see Ref. [12], and is driven by the nonlinear polarization of the Xe gas, which is derived in Section 2.3 .

2.2 Spatial and Temporal Incoherence

The front-end of the NIKE KrF light source is a spatially and temporally incoherent ASE (amplified spontaneous emission) oscillator, which can be represented by a collection of many

independent oscillators emitting at frequencies in the range of the carrier frequency, and which are scattered throughout space in such a way that the spatial frequency distribution is roughly symmetric about zero. Numerically, this is represented by a 3D function determined according to the average output of the ASE, which we model here as Gaussian in frequency and spatial frequency space and centered about $(\omega_0, 0, 0)$. Each amplitude A_{ω,k_x,k_y} (corresponding to the sum of a large collection of independent oscillators at (ω, k_x, k_y)) is thus a Gaussian-distributed complex random number with random phase. The amplitude squared $\left|A_{\omega,k_x,k_y}\right|^2$ is then multiplied by the incident power spectrum. The resulting function A_{ω,k_x,k_y} is Fourier transformed into time and space, resulting in the function $G(t, x, y)$. The function G has been normalized according to the power of the KrF beam and multiplied by a top-hat shaped filter function, which corresponds to the beam aperture.

The ASE light, which is modeled as a quasi-collimated multimode beam, traverses an aperture whose width D is ~ 75 times larger than the spatial coherence zones determined by the (k_x, k_y) angular divergence. It thus takes on the structure of a 75x75 transverse array of uncorrelated beams, each of which is mostly uncorrelated with itself after every coherence time $\tau_c = 2\pi/\Delta\omega$, where $\Delta\omega$ is the spectral bandwidth. Each uncorrelated beam is produced by a varying number of random oscillators, so that the structure can be viewed as a three-dimensional, checkered array of random Gaussian numbers with random phase (labeled as $F(t, x, y)$) which when integrated over many coherence times yields a flat-top beam profile.

Nonetheless, it will suffice to model the field envelope as $E_0 \times G(t, x, y)$, see Ref. [2]. A measurement of the initial beam profile or the far field profile can be incorporated for more accurate results.

2.3 Nonlinear Response of Xe Gas

In this section, we derive the nonlinear polarization of the Xe gas, which is the source term of the wave propagation equation, see Eq. (1).

2.3.1 Density matrix equations

The electric response of the Xe atom is modeled by the Hamiltonian $\hat{H}(\mathbf{r},t) = \hat{H}_0(\mathbf{r},t)+\hat{V}(\mathbf{r},t)$, where $\hat{H}_0(\mathbf{r},t)$ represents the unperturbed atom, $\hat{V}(\mathbf{r},t) = -\mu(\mathbf{r})\cdot\mathbf{E}(\mathbf{r},t) = -q\mathbf{r}\cdot\mathbf{E}(\mathbf{r},t)$ represents the electric dipole interaction, μ is the dipole moment operator, and $E(\mathbf{r},t) = |E_p(\mathbf{r},t)|\cos(\phi(\mathbf{r},t)) = (1/2)E_p(\mathbf{r},t)\exp(ik_0z - i\omega_0t)+c.c.$ is the classical field associated with the KrF laser light. Although the following equations can produce a nonzero third harmonic polarization, the third harmonic electric field is neglected here. This is justified because the large phase mismatch created by dispersion and cross-phase modulation strongly suppresses the convective growth of the third-harmonic field at this far UV wavelength, which is also strongly absorbed by photoionization. The slowly-varying amplitude $|E_p(\mathbf{r},t)|$ and the phase $\phi(\mathbf{r},t)$ are real, with the instantaneous frequency given by $\omega(t) = \dot{\phi}(t) = \omega_0 + \delta\omega(t)$, where $\omega_0 = 2\pi c/\lambda_0$ and $\lambda_0 = 248.4$nm. If the KrF light is linearly polarized, a two-photon near-resonance with the Xe 6p[1/2]0 state at 80119cm^{-1} (2 / 249.63nm) results in a negative nonlinear refractive index around λ_0. We write the wave function as $\Psi = \sum_n c_n(\mathbf{r},t)u_n(R)$ where $u_n(R)$ is the eigenfunction corresponding to the eigenstate $|n\rangle$ of H_0 and R is the position of the outer electron with respect to the nucleus. Although multiple odd-parity intermediate eigenstates contribute to the two-photon transition, we model a three-level system here for simplicity, where $|1\rangle$ is the 5p^6 ground state, $|2\rangle$ represents the odd-parity intermediate states,

and $|3\rangle$ is the Xe 6p[1/2]0 two-photon near-resonant state. For the closed, three-level system, the von Neumann equation $d\rho/dt = [\hat{H}, \rho]/i\hbar$ yields the following density matrix equations:

$$
\begin{aligned}
\partial\rho_{11}/\partial t =& i\left(\Omega_{12}\rho_{21} - \Omega_{21}\rho_{12}\right) + \Gamma_I(\rho_{22} - \rho_{22}^{eq}) + R\Gamma_c(\rho_{33} - \rho_{33}^{eq}),\\
\partial\rho_{22}/\partial t =& -\Gamma_I(\rho_{22} - \rho_{22}^{eq}) + i\left(\Omega_{21}\rho_{12} - \Omega_{12}\rho_{21}\right) + i\left(\Omega_{23}\rho_{32} - \Omega_{32}\rho_{23}\right) + (1-R)\Gamma_c(\rho_{33} - \rho_{33}^{eq}),\\
\partial\rho_{33}/\partial t =& -\Gamma_c(\rho_{33} - \rho_{33}^{eq}) + i\left(\Omega_{32}\rho_{23} - \Omega_{23}\rho_{32}\right),\\
\partial\rho_{12}/\partial t =& -\gamma_N\rho_{12} + i\,\omega_{21}\rho_{12} + i\,\Omega_{12}\left(\rho_{22} - \rho_{11}\right) - i\bar{\Omega}_{32}\rho_{13},\\
\partial\rho_{13}/\partial t =& -\gamma_c\rho_{13} + i\,\omega_{31}\rho_{13} + i\left(\Omega_{12}\rho_{23} - \Omega_{23}\rho_{12}\right),\\
\partial\rho_{23}/\partial t =& -\gamma_L\rho_{23} + i\,\omega_{32}\rho_{23} + i\,\Omega_{23}\left(\rho_{33} - \rho_{22}\right) + i\Omega_{21}\rho_{13}\ ,
\end{aligned}
\tag{2}
$$

where the density matrix elements are defined as $\rho_{nm}(\mathbf{r},t) = \langle n|\rho(\mathbf{r},t)|m\rangle = c_m^*(\mathbf{r},t)c_n(\mathbf{r},t)$ and where $\omega_{mn} = \omega_m - \omega_n$. The transition frequencies are defined as $\Omega_{m\,n}(\mathbf{r},t) = \langle m|\,\hat{\mu}\,|n\rangle \cdot E(\mathbf{r},t)/\hbar = \Omega^{+}_{m\,n}(\mathbf{r},t)\exp(i\phi(\mathbf{r},t)) + \Omega^{-}_{m\,n}(\mathbf{r},t)\exp(-i\phi(\mathbf{r},t))$, where $\Omega^{\pm}_{m\,n}(\mathbf{r},t) = \mu_{mn}\cdot|E_p(\mathbf{r},t)|/2\hbar$ varies slowly in time and space and $\pm$ is a carrier frequency marker; for linear polarization we take μ_{nm} to be real and express $\Omega^{+}_{m\,n}(\mathbf{r},t) \to \Omega_{mn}(\mathbf{r},t) = \mu_{mn}|E_p(\mathbf{r},t)|/2\hbar$. Equation (2) applies to a general three-level system with ground state $|1\rangle$, intermediate state $|2\rangle$, and excited state $|3\rangle$. The spatial symmetry of the Hamiltonian requires that $\Omega_{n\,n} = 0$ for each eigenstate $|n\rangle$, and we have specified the allowed transitions to be $|1\rangle \to |2\rangle \to |3\rangle$. The dynamics of inelastic collisions and spontaneous emission in the system are general, where R satisfies $0 \le R \le 1$ and describes the fraction of the energy emitted from

$|3\rangle$ that transfers directly to $|1\rangle$.

2.3.2 Parameters

For a 248.4nm laser pulse propagating through an atomic Xe gas, the two-photon excited state is the Xe 6p[1/2]0 state. For a KrF NIKE pulse, we have 600ps short pulses and 4ns long pulses, which yield a frequency scale 1.7 GHz and 0.3 GHz, respectively. The elastic collision rate at 200mbar is 0.5 GHz, and the radiative decay rate of the excited Xe state is 0.03 GHz, see Supplement.

2.3.3 Separation of density matrix elements into harmonics of the laser frequency

To simplify the notation, the spatial dependence of the field and matrix elements will be dropped here; however, it can be reincorporated in a straightforward manner. We write each element as the sum of components at roughly the various harmonics 0, $\pm\dot{\phi}(t)$, $\pm 2\dot{\phi}(t)$, $\pm 3\dot{\phi}(t)$ of the laser frequency:

$$\rho_{ij} = \sigma_{ij}(0) + \sigma_{ij}(-\phi)\exp(-i\phi) + \sigma_{ij}(\phi)\exp(i\phi) + \sigma_{ij}(-2\phi)\exp(-2i\phi) + \sigma_{ij}(2\phi)\exp(2i\phi)$$
$$+\sigma_{ij}(-3\phi)\exp(-3i\phi) + \sigma_{ij}(3\phi)\exp(3i\phi),$$

where $\sigma_{ij}(-s\phi) = [\sigma_{ji}(s\phi)]^*$. The density matrix equations are then rewritten according to Eq. (S1) for integer $s \in (-3, -2, ..., 3)$. We calculate the full nonlinear response to the first-harmonic field here, but will ultimately only include the first-harmonic polarization component in the analysis.

2.3.4 Two-photon vector model

For an ISI beam with temporal fluctuations that are much longer than the timescale associated with the detuning, e.g. $2\pi/\Delta \sim 0.2$ps where $\Delta = (2\omega_0 - \omega_{31})/2$, the off-diagonal density matrix elements are only driven significantly near the various harmonics of the laser frequency, see Supplement and Eq. (S3). In the case where damping terms can be neglected, we define a real vector $r = (r_1, r_2, r_3)$ according to $r_1 = \sigma_{13}(2\phi) + [\sigma_{13}(2\phi)]^*$, $r_2 = i(\sigma_{13}(2\phi) - [\sigma_{13}(2\phi)]^*)$, $r_3 = \sigma_{33}(0\phi) - \sigma_{11}(0\phi)$, and obtain the familiar (see Ref. [7-8]) two-photon vector model shown below. See Eq. (9) for the formulation that is used for our simulations.

$$\begin{aligned} \dot{r}_1 &= -\gamma_3 r_2 \ , \\ \dot{r}_2 &= \gamma_3 r_1 - \gamma_1 (r_3 + O(\Delta/\omega_0)) \approx \gamma_3 r_1 - \gamma_1 r_3 \ , \\ \dot{r}_3 &= \ \gamma_1 r_2 \ , \end{aligned} \tag{3}$$

where

$$\gamma_1 = \Omega_{12}\Omega_{23}\left(\frac{1}{\omega_{21}-\dot{\phi}} - \frac{1}{\omega_{32}-\dot{\phi}}\right) \approx \frac{2\,\Omega_{12}\Omega_{23}}{\omega_{21}-\dot{\phi}} = \left(\frac{\mu_{12}\mu_{23}|E_p|^2}{2\hbar^2(\omega_{21}-\dot{\phi})}\right),\ \gamma_3 = -(\omega_{31} - 2\dot{\phi} + \delta\omega_{31}),$$

$$\begin{aligned} \delta\omega_{31} &= \Omega_{12}^2\left(\frac{1}{\dot{\phi}-\omega_{32}} + \frac{1}{3\dot{\phi}-\omega_{32}}\right) + \Omega_{23}^2\left(\frac{1}{\dot{\phi}-\omega_{21}} + \frac{1}{3\dot{\phi}-\omega_{21}}\right) \\ &= |\mu_{12}E_p/2\hbar|^2\left(\frac{1}{\dot{\phi}-\omega_{32}} + \frac{1}{3\dot{\phi}-\omega_{32}}\right) + |\mu_{23}E_p/2\hbar|^2\left(\frac{1}{\dot{\phi}-\omega_{21}} + \frac{1}{3\dot{\phi}-\omega_{21}}\right). \end{aligned}$$

2.3.5 Two-photon adiabatic following approximation

When the phase and amplitude of the field envelope vary slowly with respect to the magnitude of the two-photon rotation vector γ, e.g., $|\partial v(t)/\partial t|/|v(t)| \ll |\gamma_3(t)|$, where $v(t) = E_p^2(t)r_3(t)$, Eq. (2) can be solved approximately via an adiabatic following approximation [13], and the

collective state of the Xe atoms can be expressed as:

$$
\begin{aligned}
r_1 &= \pm\gamma_1/(\gamma_1^2+\gamma_3^2)^{1/2} \\
r_3 &= \pm\gamma_3/(\gamma_1^2+\gamma_3^2)^{1/2} \\
r_2 &= \dot{r}_3/\gamma_1 = \pm\frac{\gamma_1\dot{\gamma}_3-\gamma_3\dot{\gamma}_1}{(\gamma_1^2+\gamma_3^2)^{3/2}}
\end{aligned}
\tag{4}
$$

Given the initial condition $r = (0,0,-1)$ and positive γ_3 , the lower sign is appropriate. The temporal incoherence of the NIKE laser induces large enough field fluctuations that the adiabatic following approximation condition is violated; however, the approximation is nonetheless a useful comparison. We further note that the adiabatic following approximation yields an effective modulation-instability gain that is asymmetric about the pump frequency. This is not, however, the cause of the small blue shift which appears in the $n_2(\dot{\phi})$ nonlinear response simulations, see Section 3.

2.3.6 Polarization

The total polarization is given by $\mathbf{P}(\mathbf{r},t) = N\langle\hat{\boldsymbol{\mu}}\rangle = NTr(\rho\hat{\boldsymbol{\mu}}) = N\left(\langle 2|\,\hat{\boldsymbol{\mu}}\,|1\rangle\,\rho_{12} + \langle 3|\,\hat{\boldsymbol{\mu}}\,|2\rangle\,\rho_{23} + c.c.\right)$ whose component along the linearly-polarized real field of magnitude $E(\mathbf{r},t) = |E_p(\mathbf{r},t)|\cos(\phi(\mathbf{r},t))$ can be written as

$$
P = N\left(\mu_{12}\sigma_{12}(\phi)\exp(i\phi) + \mu_{12}\sigma_{12}(3\phi)\exp(3i\phi) + \mu_{23}\sigma_{23}(\phi)\exp(i\phi) + \mu_{23}\sigma_{23}(3\phi)\exp(3i\phi)\right) + \text{c.c.}
$$

The third-harmonic polarization component is included for completeness in this expression, but is neglected in the remainder of the discussion and in the simulations.

The envelopes $\sigma_{12}(n\phi)$ and $\sigma_{23}(n\phi)$ are well approximated by their adiabatic solutions in Eq. (S2b) because the respective detunings $\left|\omega_{21} - n\dot{\phi}\right|$ and $\left|\omega_{32} - n\dot{\phi}\right|$ that appear in $\dot{\sigma}_{12}(n\phi)$ and $\dot{\sigma}_{23}(n\phi)$ (see Eq. (S1)) far exceed the damping terms γ_N and γ_L or any spectral components in $\sigma_{12}(n\phi)$ and $\sigma_{23}(n\phi)$. Applying these results, ignoring the small damping terms $\gamma_{N,\,L}$, using $\Omega_{mn}^{\pm} = \mu_{mn}\left|E_p\right|/2\hbar$, then writing $\sigma_{33}(0\phi) \simeq (1 + r_3)/2$, $\sigma_{11}(0\phi) \simeq (1 - r_3)/2$, $\sigma_{13}(2\phi) = (r_1 - ir_2)/2$, we obtain the polarization associated with the two-photon vector model:

$$\begin{aligned} P/N \simeq & -\mu_{21}(\dot{\phi} - \omega_{21})^{-1}\left[\Omega_{12}^{+}\sigma_{11}(0\phi) + \Omega_{32}^{-}\sigma_{13}(2\phi)\right]\exp(i\phi) \\ & +\mu_{32}(\dot{\phi} - \omega_{32})^{-1}\left[\Omega_{23}^{+}\sigma_{33}(0\phi) + \Omega_{21}^{-}\sigma_{13}(2\phi)\right]\exp(i\phi) + c.\,c.\,, \end{aligned} \tag{5a}$$

which becomes

$$\begin{aligned} P/N \simeq & -(2\hbar)^{-1}\left(\mu_{12}^2(\dot{\phi} - \omega_{21})^{-1}(1 - r_3) - \mu_{23}^2(\dot{\phi} - \omega_{32})^{-1}(1 + r_3)\right)\left|E_p\right|\cos(\phi) \\ & -(2\hbar)^{-1}\mu_{12}\mu_{23}\left((\dot{\phi} - \omega_{21})^{-1} - (\dot{\phi} - \omega_{32})^{-1}\right)\left|E_p\right|\left(r_1\cos(\phi) + r_2\sin(\phi)\right)\,, \end{aligned} \tag{5b}$$

where we have defined the matrix elements $\mu_{12} = \mu_{21}$ and $\mu_{23} = \mu_{32}$ to be real, and ignored all even harmonic terms except $\sigma_{13}(2\phi)$. Using the two-photon adiabatic following approximation of Eq. (4) and neglecting the small damping term $r_2 \propto \dot{\gamma}_1\,,\ \dot{\gamma}_3\,$, we obtain

$$\begin{aligned} & P/N \simeq -(2\hbar)^{-1}(\gamma_1^2 + \gamma_3^2)^{-1/2}\times \\ & \left(\begin{array}{l} \mu_{12}^2(\dot{\phi} - \omega_{21})^{-1}((\gamma_1^2 + \gamma_3^2)^{1/2} + \gamma_3) - \mu_{23}^2(\dot{\phi} - \omega_{32})^{-1}((\gamma_1^2 + \gamma_3^2)^{1/2} - \gamma_3) \\ -\mu_{12}\mu_{23}\gamma_1\left((\dot{\phi} - \omega_{21})^{-1} - (\dot{\phi} - \omega_{32})^{-1}\right) \end{array}\right)\left|E_p\right|\cos(\phi)\,. \end{aligned} \tag{5c}$$

In the small field limit where $\gamma_3 \gg \gamma_1$, this reduces to

$$P/N \approx \left(-\frac{\mu_{12}^2}{(\dot{\phi}-\omega_{21})\hbar} - |E_p|^2 \frac{\mu_{12}^2 \mu_{23}^2}{8\hbar^3} \times \left(\frac{1}{\dot{\phi}-\omega_{21}} - \frac{1}{\dot{\phi}-\omega_{32}} \right)^2 \left(\frac{1}{2\dot{\phi}-\omega_{31}} \right) \right) |E_p| \cos(\phi) \ . \tag{5d}$$

The polarization has the usual linear, DC terms as well as the nonlinear terms at the laser frequency. We can obtain Eq. (5d) for the nonlinear polarization alternatively by expanding the density matrix elements in powers of the field amplitude, see Ref. [6].

From (5d), we obtain the following expression for the nonlinear refractive index:

$$\tilde{n}_2(\omega_0) = \frac{N\mu_{12}^2\mu_{23}^2}{4\varepsilon_0 n_0 \hbar^3 (\omega_{31}-2\omega_0)(\omega_{21}-\omega_0)^2} \tag{6}$$

and the nonlinear polarization is given by

$$P_{NL,p}(t) = \left(2\varepsilon_0 n_0 \tilde{n}_2 \left(\dot{\phi}(t) \right) |E_p(t)|^2 \right) E_p(t), \tag{7}$$

where $E(t) = (1/2)E_p(t)\exp(-i\omega_0 t) + c.c. = |E_p(t)|\cos(\phi(t))$, and

$P_{NL}(t) = (1/2)P_{NL,p}(t)\exp(-i\omega_0 t) + c.c.$.

This result is obtained from the first-harmonic term of the nonlinear polarization and is consistent with the nonlinear index derived in Ref. [3,17], according to $\tilde{n}_2 = (1/2)\tilde{n}_{2,\text{alt}} = (1/8\pi)\tilde{n}_{2,\text{alt,cgs}}$ where $\tilde{n}_{2,\text{alt}}$ is defined according to $\varepsilon = \left(n_0 + \tilde{n}_{2,\text{alt}} \left\langle {E_p}^2 \right\rangle\right)^2 - 1 = \left(n_0 + 2\tilde{n}_2 |E_p|^2\right)^2 - 1$ where the time-averaged field magnitude $\left\langle {E_p}^2 \right\rangle = |E_p|^2/2$ and the subscript 'cgs' refers to cgs units. We note that it has been derived in the small field limit under the two-photon adiabatic following approximation.

In the more general case, i.e. Eq. (5b), the nonlinear polarization $P_{NL}(t) = (1/2)P_{NL,p}(t)\exp(-i\omega_0 t) + c.c.$ can be expressed as shown below (see Supplement for a discussion of the additional intermediate levels):

$$P_{NL,p}(t)/E_p(t) = (N/2\hbar)\begin{pmatrix} \mu_{12}(\omega_{21} - \dot{\phi} - i\gamma_N)^{-1}(\,\mu_{23}\rho_Z - \mu_{12}(1+r_3)) \\ \\ -\mu_{23}(\,\omega_{32} - \dot{\phi} - i\,\gamma_L)^{-1}(\mu_{23}(1+r_3) + \mu_{12}\rho_Z) \end{pmatrix},$$

where $\rho_Z = 2\sigma_{13}(2\phi)^* = (r_1 + ir_2)$, and Eq. (3) gives

$$\mathrm{d}\rho_Z/\mathrm{d}t = i\gamma_3\rho_Z - i\gamma_1 r_3,$$

$$\mathrm{d}r_3/\mathrm{d}t = \gamma_1 r_2 = i\gamma_1(\rho_Z^* - \rho_Z)/2 = i\gamma_1\rho_Z^*/2 + cc,$$

$$\gamma_1 = \Omega_{12}\Omega_{23}(\frac{1}{\omega_{21} - \dot{\phi}} - \frac{1}{\omega_{32} - \dot{\phi}}) = \frac{\mu_{12}\mu_{23}}{\hbar^2}|E_p/2|^2(\frac{1}{\omega_{21} - \dot{\phi}} - \frac{1}{\omega_{32} - \dot{\phi}}) \text{ , and}$$

$$\gamma_3 = -(\omega_{31} - 2\dot{\phi} + \delta\omega_{31}) \approx -(\omega_{31} - 2\dot{\phi}).$$

We note that the $(1 - r_3)$ term has been rewritten as $2 - (1 + r_3)$. The first term represents the contribution to the linear index of refraction (approximately $\delta n_0 \sim 5 \times 10^{-4}$) and has been eliminated in order to yield the expression for $P_{NL,p}(t)$.

Alternatively, we can write the nonlinear polarization as

$$
\begin{aligned}
P_{NL,p}(t)/E_p(t) = (N/2\hbar) & \begin{pmatrix} \mu_{12}(\omega_{21} - \dot{\phi} - i\gamma_N)^{-1}(\,\mu_{23}\rho_L) \\ \\ -\mu_{23}(\,\omega_{32} - \dot{\phi} - i\,\gamma_L)^{-1}(\mu_{12}\rho_L) \end{pmatrix} \frac{E_p^*(t)}{E_p(t)} \\
+(N/2\hbar) & \begin{pmatrix} \mu_{12}(\omega_{21} - \dot{\phi} - i\gamma_N)^{-1}(-\mu_{12}(1+r_3)) \\ \\ -\mu_{23}(\,\omega_{32} - \dot{\phi} - i\,\gamma_L)^{-1}(\mu_{23}(1+r_3)) \end{pmatrix} ,
\end{aligned}
\tag{8}
$$

where $\rho_L = (r_1 + ir_2)\exp(2i\omega_0 t - 2i\phi(t))$, and

$$
\begin{aligned}
&\mathrm{d}\rho_L/\mathrm{d}t = i\gamma'_3\rho_L - i\gamma'_1 r_3, \\
&\mathrm{d}r_3/\mathrm{d}t = i\gamma'_1\rho_L^*/2 + c.c. = \mathrm{Im}[(\gamma'_1)^*\rho_L] \\
&\gamma'_1 = \frac{\mu_{12}\mu_{23}}{\hbar^2}(E_p/2)^2\left(\frac{1}{\omega_{21}-\omega_0} - \frac{1}{\omega_{32}-\omega_0}\right) , \text{ and} \\
&\gamma'_3 = -(\omega_{31} - 2\omega_0 + \delta\omega_{31}) \approx -(\omega_{31} - 2\omega_0).
\end{aligned}
\tag{9}
$$

This latter form is preferable from a numerical standpoint because the instantaneous frequency $\dot{\phi}$ of a temporally incoherent laser tends to fluctuate wildly over short timescales, i.e., a much higher temporal resolution is required to resolve ρ_Z than to resolve ρ_L.

In the case of negligible population redistribution, Eq. (9) can be expressed by a single, driven harmonic oscillator equation given by

$$
(\partial/\partial t - i\gamma'_3)\,\rho_L = i\gamma'_1 \tag{10}
$$

and solved exactly, i.e.,

$$\rho_L(t) = \rho_L(t_0) \exp\left(i \int_{t_0}^{t} \gamma_3'(t')dt' \right) \int_{t_0}^{t} dt'' i\gamma_1'(t'') \exp\left(i \int_{t''}^{t} \gamma_3'(t')dt' \right) .$$

This solution can be evaluated more simply in frequency space, i.e., $\tilde{\rho}_L = i\tilde{\gamma}_1'/(i\omega - i\gamma_3')$.

2.4 Numerical Techniques

The generalized Nonlinear Schrodinger Equation, see Eq. (1), is integrated along the propagation axis via a split-step method, where the diffraction term has been incorporated into the dispersive propagator and where calculation of the nonlinear propagator is parallelizable.

The nonlinear polarization of Xe gas according to the two-photon vector model can be calculated most generally via numerical time integration of the coupled first order equations $\mathrm{d}r_3/\mathrm{d}t$ and $\mathrm{d}\rho_L/\mathrm{d}t$ in Eq. (9) according to a straightforward iterative scheme - or in the case of negligible population redistribution Eq. (10). In the latter case, we opt for the straightforward frequency domain solution discussed above, which is an order of magnitude faster. Doing so requires that a small imaginary component be added to γ_3' to prevent divergent behavior.

The instantaneous frequency at time t is not required in our formulation of the two-photon vector model, see Eq. (8), but it can be calculated by taking the derivative of the phase of the electric field envelope having accounted for 2π phase jumps. Alternatively, it can be calculated by locating the spectral peak of the Fourier Transform of the product of the field envelope and a narrow Gaussian centered about time t. The instantaneous frequency is used to calculate the nonlinear source term for the $n_2(\dot{\phi})$ response model given in Eq. (6-7).

The input condition for the generalized Nonlinear Schrodinger Equation is discussed in Section 2.2. The filter function generating the top-hat beam shape is constructed from two hyperbolic tangent functions.

Guard bands are employed to absorb all energy beyond some frequency threshold, thereby avoiding aliasing across the periodic boundary imposed by the Fast Fourier Transform operation as well as eliminating any high-frequency artifacts which arise from the numerical integration of the coherence term. Any error (especially for a longer pulse) in the numerical integration can slightly violate the energy conservation condition $\int_{-T/2}^{T/2} \left|\hat{E}(t,x,y)\right|^2 r_2(t,x,y)dt = 0$ which is valid in the limit that $\Gamma_c T \ll 1$. To address this concern, r_2 is shifted accordingly upward or downward by a very small, smooth plateau of the pulse width T after each integration step. The necessary resolution along the propagation axis can be reduced by splitting the growth/decay part nonlinear propagator into smaller, energy-conserving steps, i.e. $\exp(\alpha r_2 \Delta z) \approx \sum_n \left(\sqrt{1+\alpha r_2 \Delta z/n}\right)^{2n}$. Grid resolution requirements in both vector spaces are imposed as well.

3 Numerical Results

The propagation of a temporally and spatially incoherent KrF laser beam through a chamber of 200mbar Xe gas is simulated in this section. The simulation parameters are listed in Table 3 and correspond to the incident beam in Ref. [2]. The times diffraction limit is varied in Figure 17.

Fig. 16-17 are simulated according to Eq. (1). The nonlinear polarization for the TPVM in Fig. 16 is determined by solving Eq. (10) in frequency space; to determine it according to Eq.

Table 2: **Simulation parameters for Fig. 16-17**

KrF Beam/Xe Property	Value
Laser wavelength	$\lambda_0 = 9.55$ μm
Peak power	33 GW
Beam size	15 cm $\times$ 15 cm
Transverse coherence length	0.5 cm (i.e. times-diffraction-limit $M_x^2 = 30$)
Pulse length	>10ps
Pulse temporal shape	Gaussian
Pulse transverse spatial shape	Flat-top beam with smoothed edges
Linewidth	1 THz
Detuning of $2\omega_0$ from two-photon resonance	11.9 THz
[a]Nonlinear refractive index at ω_0	-190 $\times$ 10^{-19} cm^2/W
Group velocity dispersion coefficient	8.2 $\times$ 10^{-6} ps^2/cm

[a]Ref. [5]. This value may be a 15-20% overestimate, see Ref. [3]

(9) yields the same result because population inversion is small. The nonlinear polarization in the second model in Fig. 16 is determined according to Eq. (6-7), and the nonlinear polarization in the third model in Fig. 16 is the instantaneous Kerr nonlinearity, also referred to here as the steady-state solution. Each data point in Fig. 17 is simulated also according to Eq. (1), for its own, noise-generated incident beam with the specified times-diffraction-limit. To clarify the physical behavior, the nonlinear polarization used in Fig. 17 has been determined according to the steady-state as opposed to Eq. (6-7); the trends and conclusions, however, are the same.

We obtain the following results, in which the coherence time is estimated according to the expression $t_c = \int (P(\nu))^2 d\nu$ where $P(\nu)$ is the normalized total power spectrum of the beam, i.e., $\int P(\nu) d\nu = 1$. This enables the calculation of a spectral broadening factor defined as SBF $= t_c(0)/t_c(z)$, where z is the propagation distance. Similarly, to quantify the

broadening of the far-field profile (whose shape is identical to the near-field transverse spatial frequency spectrum), we substitute it into the 2D spatial version of the t_c expression to calculate the near-field transverse coherence zone radius r_c; this gives the far-field broadening factor FFBF $= r_c(0)/r_c(z)$. This factor is essentially unchanged if we use the 1D (along the x-axis) spatial version of the t_c expression. The small broadening of the near-field profile itself can be estimated by the beam spread factor BSF $= 1 + (k_\perp/k_0)z/D$, where $k_\perp/k_0$ is the beam spreading angle, $k_\perp$ is the spatial frequency version of r_c, and $D = 15$ cm is the beam width. The small beam spread arises in part due to the ISI beam divergence and in part due to the effects of the nonlinear far field broadening.

The amount of spectral broadening seen in Fig. 16 for 50m of 200mbar Xe is comparable to that seen in Ref. [2] for beam propagation through a 100m air path.

The transverse spatial behavior in Fig. 16 is independent of whether the nonlinearity is calculated according to the TPVM, Kerr response, or instantaneous Kerr response. The spectral behavior, however, is model-dependent. The TPVM displays a reduction in high frequencies; its difference with respect to the delayed Kerr response can be attributed to the large field fluctuations, which render inaccurate the step used to obtain Eq. (5c) (in which the adiabatic following approximation was applied and the $\dot{\gamma}_i$ term was neglected).

Additionally, we find that the population redistribution and collisional damping are too small for any decrease in the amount of spectral broadening to be observed.

Since the simulations are only for a 30 times-diffraction-limited beam (due to computational constraints), it is useful to consider how the propagation properties of a 75 times-diffraction-limited beam will differ, see Fig. 17. The spectral broadening factor (SBF) is

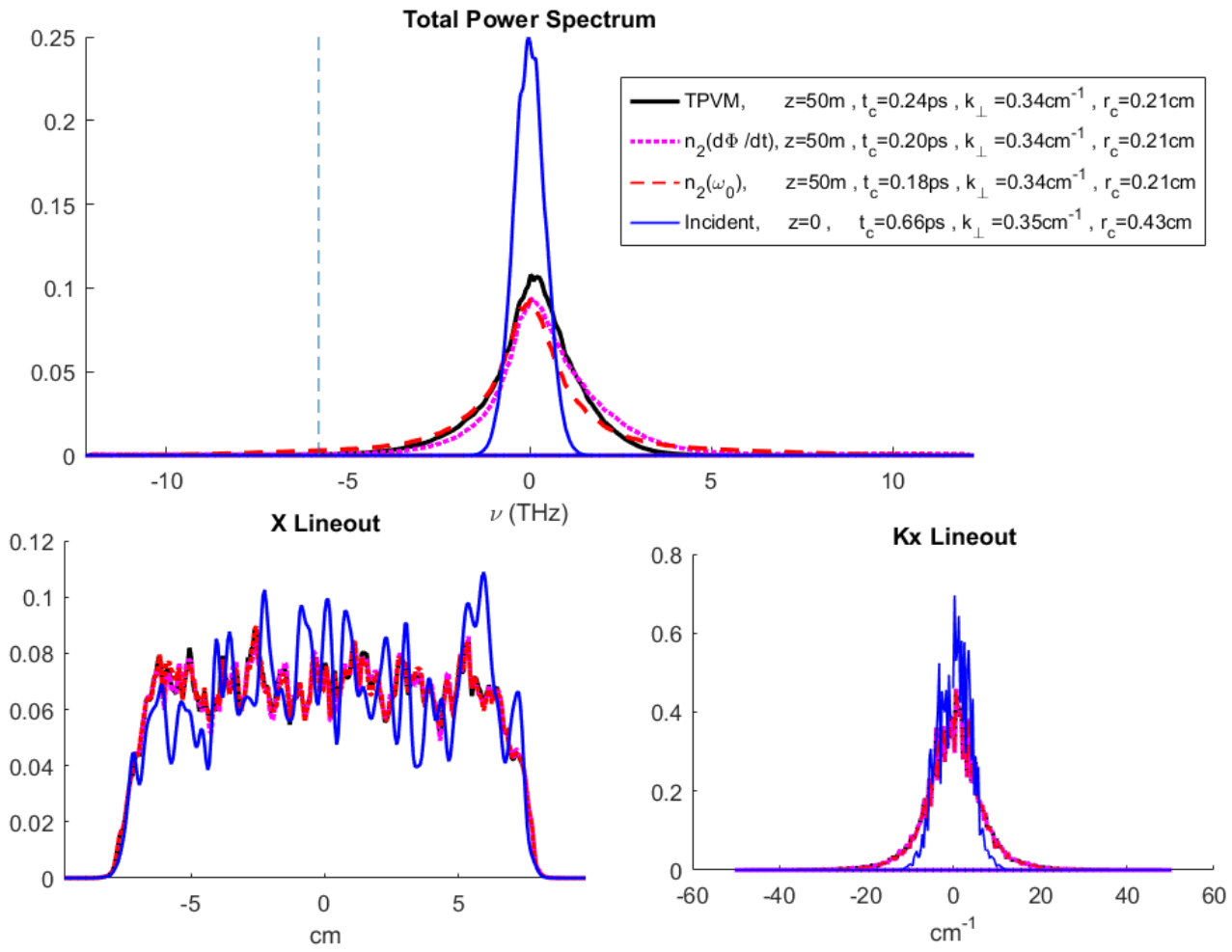

Figure 16: Propagation of a 30 M_x^2 (times-diffraction-limit) temporally and spatially incoherent KrF laser beam through 50m of 200mbar Xe gas, see Table 2: (a) Total power spectrum (b) Axial lineout of near-field beam profile (c) Axial lineout of far-field beam profile , modeled via the Two-Photon Vector Model (TPVM) using either Eq. (9) or Eq. (10), the Kerr response $n_2(\dot{\phi}(t))$ see Eq. (6-7), and the narrow-bandwidth, steady-state Kerr response $n_2(\omega_0)$. Properties of the incident light (z=0) are indicated in black.

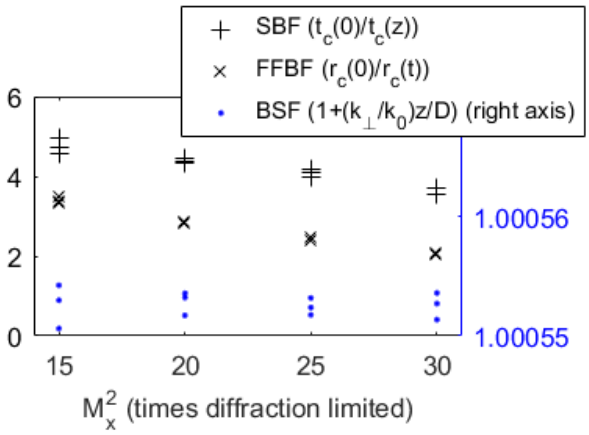

Figure 17: Spectral Broadening Factor, Far-field Broadening Factor, Beam Spreading Factor are plotted as a function of the times-diffraction-limit (M_x^2), for propagation of a temporally and spatially incoherent KrF laser beam through 50m of 200mbar Xe gas.

reduced as M_x^2 increases, as is the far-field broadening factor (FFBF). These effects can be attributed to the phase mismatch of the 3D wave vectors involved in four wave mixing, or equivalently, the interruption of amplification paths. For a smaller spot size, the beam spreading factor (BSF) can become significant and increase with M_x^2, such that the SBF and FFBF decrease more significantly with M_x^2 than in Fig. 17 and roughly in proportion to $(1 + M_x^2/a)^{-2}$, where a is some constant. The BSF in Fig. 17 is due to the effects of far-field broadening, roughly an order of magnitude larger than it would be due to ISI beam divergence alone. Its slight decrease with M_x^2 appears not to be a statistical anomaly, but rather a nonlinear effect occurring in the regime where the nonlinear index and the group velocity dispersion coefficient have opposite signs.

It is expected (for the parameters in Table 2) that at 75 times-diffraction-limit the SBF will be roughly 2, and that the FFBF will be less than that, see Fig. 17. It must be noted, however, that the nonlinearity may be overestimated by 15-20%, see Table 2. The SBF is larger than the FFBF in Fig. 17 which we have seen in simulations is in part due to the four

wave mixing phase mismatch mentioned above, but can be mostly attributed to the positive group velocity dispersion coefficient, which in a negative-n_2 medium sharpens the pulse in time, thereby increasing the rate of spectral broadening.

4 Discussion

We have shown that propagation of the KrF NIKE laser output beams through Xe gas may be an effective way of increasing the laser bandwidth beyond that which can be achieved via propagation through air. The beam spreading factor is sufficiently small. The far-field broadening factor is significant, though it is at least smaller than the spectral broadening factor which has been enhanced by group velocity dispersion. Far-field broadening may limit the propagation distance and thus the spectral broadening that can be achieved. The best way to maximize the spectral broadening while limiting the degradation of the far-field beam profile is likely propagation through a chamber containing both air and Xe.

5 Conclusions

The nonlinear response of Xe gas to chaotic non-steady-state, near-resonance light has been modeled using a two-photon vector model. The propagation of the KrF NIKE laser light through 200mbar Xe has been simulated, and a dependence of the spectral broadening and beam profile degradation on the times-diffraction-limit is observed and discussed. The results of the TPVM are compared with those of a delayed response model and an instantaneous response model. We conclude that propagation of the KrF NIKE laser output beams through

Xe may be an effective way of increasing the laser bandwidth, thereby suppressing the laser-plasma instabilities.

6 References

[1] Obenschain, S., Lehmberg, R., Kehne, D., Hegeler, F., Wolford, M., Sethian, J., Weaver, J. and Karasik, M., 2015. High-energy krypton fluoride lasers for inertial fusion. Applied optics, 54(31), pp.F103-F122.

[2] Weaver, J., Lehmberg, R., Obenschain, S., Kehne, D. and Wolford, M., 2017. Spectral and far-field broadening due to stimulated rotational Raman scattering driven by the Nike krypton fluoride laser. Applied optics, 56(31), pp.8618-8631.

[3] Lehmberg, R. H., C. J. Pawley, A. V. Deniz, M. Klapisch, and Y. Leng. "Two-photon resonantly-enhanced negative nonlinear refractive index in xenon at 248 nm." Optics communications 121, no. 1-3 (1995): 78-88.

[4] Betti, R., and O. A. Hurricane. "Inertial-confinement fusion with lasers." Nature Physics 12, no. 5 (2016): 435.

[5] Nibbering, E. T. J., G. Grillon, M. A. Franco, B. S. Prade, and André Mysyrowicz. "Determination of the inertial contribution to the nonlinear refractive index of air, N 2, and O 2 by use of unfocused high-intensity femtosecond laser pulses." JOSA B14, no. 3 (1997): 650-660.

[6] Lehmberg, R. H., J. Reintjes, and R. C. Eckardt. "Negative nonlinear susceptibility of cesium vapor around 1.06 μm." Physical Review A 13, no. 3 (1976): 1095.

[7] Grischkowsky, D., M. M. T. Loy, and P. F. Liao. "Adiabatic following model for two-photon transitions: nonlinear mixing and pulse propagation." Physical Review A 12, no. 6 (1975):

2514.

[8] Grischkowsky, D. "Coherent excitation, incoherent excitation, and adiabatic states." Physical Review A 14, no. 2 (1976): 802.

[9] Lehmberg, R. H., and S. P. Obenschain. Use of Induced Spatial Incoherence for Uniform Illumination on Laser Fusion Targets. No. NRL-MR-5029. Naval Research Lab, Washington DC, 1983.

[10] Lehmberg, R. H., A. J. Schmitt, and S. E. Bodner. "Theory of induced spatial incoherence." Journal of applied physics 62, no. 7 (1987): 2680-2701.

[11] Brabec, Thomas, and Ferenc Krausz. "Nonlinear optical pulse propagation in the single-cycle regime." Physical Review Letters 78, no. 17 (1997): 3282.

[12] Taha, Thiab R., and Mark I. Ablowitz. "Analytical and numerical aspects of certain nonlinear evolution equations. II. Numerical, nonlinear Schrodinger equation." Journal of Computational Physics 55, no. 2 (1984): 203-230.

[13] Crisp, M.D. "Adiabatic-Following Approximation." Physical Review A 8, no. 4 (1973): 2128.

[14] Junnarkar, Mahesh R., and Naoshi Uesugi. "Near-two-photon-resonance short-pulse propagation in atomic xenon." Optical Pulse and Beam Propagation. Vol. 3609. International Society for Optics and Photonics, 1999.

[15] Gornik, W., et al. "Two-photon excitation of xenon atoms and dimers in the energy region of the 5 p 56 p configuration." The Journal of Chemical Physics 75.1 (1981): 68-74.

[16] Bruce, M. R., et al. "Radiative lifetimes and collisional deactivation of two-photon excited xenon in argon and xenon." The Journal of chemical physics 92.5 (1990): 2917-2926. [17]

Grischkowsky, D. and Armstrong, J.A., 1972. Self-defocusing of light by adiabatic following in rubidium vapor. Physical Review A, 6(4), p.1566.

7 Supplement

Parameters

For a 248.4nm laser pulse propagating through an atomic Xe gas, the two-photon excited state is the Xe 6p[1/2]0 state, and a classical collisional model predicts an elastic collision rate of $\gamma_c \sim 4P\pi r_{Xe}^2\sqrt{2/m_{\mathrm{Xe}}kT} = 2.4\mathrm{GHz} \times (\mathrm{P/bar})$ where P is the pressure of the Xe gas, T is the gas temperature, and m_{Xe} and r_{Xe} are the mass and van der Waals radius of an individual Xe molecule. We estimate the spontaneous emission rates as $\mathrm{A}_{32} = |\mu_{32}|^2\omega_{32}^3/(3\pi\varepsilon_0\hbar c^3) \approx 40\mathrm{MHz}$ and $\mathrm{A}_{21} = |\mu_{21}|^2\omega_{21}^3/(3\pi\varepsilon_0\hbar c^3) \approx 5\mathrm{GHz}$ (see Ref. [14]). The FWHM of the two-photon absorption spectrum given a laser linewidth $\Delta\omega_L = 2.9\mathrm{GHz}$ is measured to be $\Delta\nu_{FWHM} = 4.6 + 3.5(P/\mathrm{bar})\mathrm{GHz} \approx \sqrt{\Delta\nu_L^2 + \Delta\nu_D^2} + \gamma_c$ (see Ref. [15]), where the Doppler broadening linewidth $\Delta\nu_D = 2\nu_0(2k_BT\ln 2/m_{Xe})^{1/2}/c \approx 1.3\mathrm{GHz}$ and the elastic collision rate $\gamma_c \sim 4P\pi r_{Xe}^2\sqrt{2/m_{\mathrm{Xe}}kT} = 2.4\mathrm{GHz} \times (\mathrm{P/bar})$ are in agreement with the experimental result. The radiative rate of the excited Xe state is measured to be $\sim$ 30 MHz (see Ref. [16]), which is consistent with the limiting spontaneous emission rate of 40 MHz. For a KrF NIKE pulse, the 600ps short pulses and 4ns long pulses correspond to a frequency scale 1.7 GHz and 0.3 GHz, respectively. The elastic collision rate at 200mbar is 0.5 GHz, and the inelastic collision rate is presumably at least an order of magnitude smaller.

Density Matrix Equations

The density matrix equations given in Eq. (1) can be rewritten for integer $s \in (-3, -2, ..., 3)$.

$$
\begin{aligned}
\dot{\sigma}_{11}(s\phi) &= (-is\dot{\phi} - \Gamma_o)\sigma_{11}(s\phi) + \delta_s\Gamma_0\rho_{11}^{eq} + a\Gamma_I(\sigma_{22}(s\phi) - \delta_s\rho_{22}^{eq}) + ab\Gamma_c(\sigma_{33}(s\phi) - \delta_s\rho_{33}^{eq}) \\
&\quad + \sum_{\pm} i\left[\Omega_{12}^{\pm}\sigma_{21}(\phi(s \mp 1)) - \Omega_{21}^{\pm}\sigma_{12}(\phi(s \mp 1))\right] , \\
\dot{\sigma}_{22}(s\phi) &= (-is\dot{\phi} - \Gamma_I)\sigma_{22}(s\phi) + \delta_s\Gamma_I\rho_{22}^{eq} + a(1-b)\Gamma_c(\sigma_{33}(s\phi) - \delta_s\rho_{33}^{eq}) \\
&\quad + \sum_{\pm} i\left(\Omega_{21}^{\pm}\sigma_{12}(\phi(s \mp 1)) - \Omega_{12}^{\pm}\sigma_{21}(\phi(s \mp 1)) + \Omega_{23}^{\pm}\sigma_{32}(\phi(s \mp 1)) - \Omega_{32}^{\pm}\sigma_{23}(\phi(s \mp 1)\right) , \\
\dot{\sigma}_{33}(s\phi) &= (-is\dot{\phi} - \Gamma_c)\sigma_{33}(s\phi) + \delta_s\Gamma_c\rho_{33}^{eq} + \sum_{\pm} i\left[\Omega_{32}^{\pm}\sigma_{23}(\phi(s \mp 1)) - \Omega_{23}^{\pm}\sigma_{32}(\phi(s \mp 1))\right] , \\
\dot{\sigma}_{12}(s\phi) &= (-is\dot{\phi} + i\,\omega_{21} - \,\gamma_N)\sigma_{12}(s\phi) + \sum_{\pm} i\,\left(\Omega_{12}^{\pm}\left[\sigma_{22}(\phi(s \mp 1)) - \sigma_{11}(\phi(s \mp 1))\right] - \Omega_{32}^{\pm}\sigma_{13}(\phi(s \mp 1))\right) , \\
\dot{\sigma}_{13}(s\phi) &= (-is\dot{\phi} + i\,\omega_{31} - \,\gamma_c)\sigma_{13}(s\phi) + \sum_{\pm} i\,\left[\Omega_{12}^{\pm}\sigma_{23}(\phi(s \mp 1)) - \Omega_{23}^{\pm}\sigma_{12}(\phi(s \mp 1))\right] , \\
\dot{\sigma}_{23}(s\phi) &= (-is\dot{\phi} + i\,\omega_{32} - \,\gamma_L)\sigma_{23}(s\phi) + \sum_{\pm} i\,\left(\Omega_{23}^{\pm}\left(\sigma_{33}(\phi(s \mp 1)) - \sigma_{22}(\phi(s \mp 1))\right) + \Omega_{21}^{\pm}\sigma_{13}(\phi(s \mp 1))\right) .
\end{aligned}
\tag{S1}
$$

Two-Photon Vector Model

On a timescale that is much longer than the inverse of the detuning $2\pi/\Delta \sim 0.2$ps where $\Delta = (2\omega_0 - \omega_{31})/2$, the off-diagonal density matrix elements will be significantly driven only near the various harmonics of the laser frequency. This means the components $\sigma_{mn}(s\phi)$ can be taken to be slowly varying in time, i.e., $|\dot{\sigma}_{mn}(s\phi)| \,/\, |\omega_0\sigma_{mn}(s\phi)| \sim \left|(\omega_{31} - 2\dot{\phi})\right| /\omega_0 = |\Delta| /\omega_0 \ll 1$. In the given case where each one-photon transition is off-resonance, this allows us to take, to zeroth order in Δ/ω_0 , $|\dot{\sigma}_{12}(s\phi)| \ll \left|(-is\dot{\phi} + i\,\omega_{21} - \,\gamma_N)\sigma_{12}(s\phi)\right|, |\dot{\sigma}_{23}(s\phi)| \ll$

$\left|(-is\dot{\phi} + i\,\omega_{32} - \ \gamma_L)\sigma_{23}(s\phi)\right|$. In this case it is also reasonable to neglect the population of the intermediate state σ_{22} because it is driven off-resonance and is to second order in the field. Since the timescale of the pulse may be comparable to or shorter than the average elastic collision time, there are non-negligible transient components of ρ_{12} and ρ_{23} as well. However, these components are non-resonant with the harmonics of the laser frequency and thus represent only a contribution to the linear response.

The near-resonance components $\sigma_{11}(0), \sigma_{33}(0), \sigma_{13}(2\phi)$ can be identified as the ones which drive other elements and contribute significantly to the polarization field. Simplifying the expression and redefining the eigenstates such the dipole moments $\mu_{12} = \mu_{21}$ and $\mu_{23} = \mu_{32}$ are real, we obtain, for linear polarization:

$$\Omega_{12}^{+\,*} = \left[\Omega_{12}^{-}\right] = \Omega_{12}^{+} \to \Omega_{12},\ \Omega_{23}^{+} \to \Omega_{23}\ ,\ \text{and} \tag{S2a}$$

$$\begin{aligned}
\sigma_{12}(s\phi) &\approx (s\dot{\phi} - \ \omega_{21} - i\gamma_N)^{-1} \sum_{\pm} \left[\Omega_{12}\left(\sigma_{11}(\phi(s \mp 1))\right) + \Omega_{32}\sigma_{13}(\phi(s \mp 1))\right]\ , \\
\sigma_{23}(s\phi) &\approx (-s\dot{\phi} + \ \omega_{32} + \ i\gamma_L)^{-1} \sum_{\pm} \left[\Omega_{23}\sigma_{33}(\phi(s \mp 1)) + \Omega_{21}\sigma_{13}(\phi(s \mp 1))\right]\ , \\
\dot{\sigma}_{13}(2\phi) &= A\sigma_{13}(2\phi) + B\sigma_{11}(0\phi) + C\sigma_{33}(0\phi)\ , \\
\dot{\sigma}_{11}(0\phi) &= E\sigma_{13}(2\phi) + c.c. + F\sigma_{11}(0\phi) + c.c. + G\sigma_{33}(0\phi) + c.c. + H\ , \\
\dot{\sigma}_{33}(0\phi) &= J\sigma_{13}(2\phi) + c.c. + L\sigma_{33}(0\phi) + c.c. + M,
\end{aligned} \tag{S2b}$$

where $E = B$ and $J = C$ from Eq. (S2a), and

$$A = (i(\omega_{31} - 2\dot{\phi}) - \ \gamma_c) - \Omega_{12}^2 \left(\frac{1}{i\dot{\phi} - i\,\omega_{32} + \ \gamma_L} + \frac{1}{3i\dot{\phi} - i\,\omega_{32} + \ \gamma_L} \right)$$
$$-\Omega_{23}^2 \left(\frac{1}{i\dot{\phi} - i\,\omega_{21} + \gamma_N} + \frac{1}{3i\dot{\phi} - i\,\omega_{21} + \gamma_N} \right) ,$$

$$B = -\Omega_{12}\Omega_{23}(i\dot{\phi} - i\,\omega_{21} + \gamma_N)^{-1} ,$$

$$C = -\Omega_{12}\Omega_{23}(i\dot{\phi} - i\,\omega_{32} + \ \gamma_L)^{-1} ,$$

$$E = -\Omega_{12}\Omega_{23}(i\dot{\phi} - i\,\omega_{21} + \gamma_N)^{-1} = B \quad ,$$

$$F = -\Gamma_o/2 - \Omega_{12}^2(i\dot{\phi} - i\,\omega_{21} + \gamma_N)^{-1} - \Omega_{12}^2(-i\dot{\phi} - i\,\omega_{21} + \gamma_N)^{-1} ,$$

$$G = +ab\Gamma_c/2 ,$$

$$H = \Gamma_0\rho_{11}^{eq} - ab\Gamma_c\rho_{33}^{eq} ,$$

$$J = -\Omega_{12}\Omega_{23}(i\dot{\phi} - i\,\omega_{32} + \ \gamma_L)^{-1} = C \quad ,$$

$$L = -\Gamma_c/2 - \Omega_{23}^2(i\dot{\phi} - i\,\omega_{32} + \ \gamma_L)^{-1} - \Omega_{23}^2(-i\dot{\phi} - i\,\omega_{32} + \ \gamma_L)^{-1} ,$$

$$M = \Gamma_c\rho_{33}^{eq} .$$

Defining a real vector $r = (r_1, r_2, r_3)$ where $r_1 = \sigma_{13}(2\phi) + [\sigma_{13}(2\phi)]^*$, $r_2 = i(\sigma_{13}(2\phi) - [\sigma_{13}(2\phi)]^*)$, $r_3 = \sigma_{33}(0\phi) - \sigma_{11}(0\phi)$, we can rewrite Eq. (S2b) to zeroth order in Δ/ω_0 as

$$
\begin{aligned}
\dot{r}_1 &= A(r_1 - ir_2)/2 + c.c. - \Omega_{12}\Omega_{23}\left[\frac{\gamma_N}{\left(\dot{\phi} - \omega_{21}\right)^2 + \gamma_N^2}(1 - r_3) + \frac{\gamma_L}{\left(\dot{\phi} - \omega_{32}\right)^2 + \gamma_L^2}(1 + r_3)\right] , \\
\dot{r}_2 &= i\left(A(r_1 - ir_2)/2\right) + c.c. - \Omega_{12}\Omega_{23}\left[\frac{\dot{\phi} - \omega_{21}}{\left(\dot{\phi} - \omega_{21}\right)^2 + \gamma_N^2}(1 - r_3) + \frac{\dot{\phi} - \omega_{32}}{\left(\dot{\phi} - \omega_{32}\right)^2 + \gamma_L^2}(1 + r_3)\right] , \\
\dot{r}_3 &= -i\Omega_{12}\Omega_{23}\left(\frac{1}{\omega_{32} - \dot{\phi} + i\gamma_L} - \frac{1}{\omega_{21} - \dot{\phi} + i\gamma_N}\right)(r_1 - ir_2)/2 + c.c. \\
&\quad + \left(\Gamma_0/2 + \gamma_N\Omega_{12}^2\left(\frac{1}{\left(\dot{\phi} - \omega_{21}\right)^2 + \gamma_N^2} + \frac{1}{\left(\dot{\phi} + \omega_{21}\right)^2 + \gamma_N^2}\right)\right)(1 - r_3) + (\Gamma_c(1 + ab)\rho_{33}^{eq} - \Gamma_0\rho_{11}^{eq}) \\
&\quad + \left(-(1 + ab)\Gamma_c/2 - \gamma_L\Omega_{23}^2\left(\frac{1}{\left(\dot{\phi} - \omega_{32}\right)^2 + \gamma_L^2}\frac{1}{\left(\dot{\phi} + \omega_{32}\right)^2 + \gamma_L^2}\right)\right)(1 + r_3) ,
\end{aligned}
\tag{S3}
$$

where we have made the replacements: $\sigma_{13}(2\phi) = (r_1 - ir_2)/2$, $\sigma_{11}(0\phi) \simeq (1 - r_3)/2$, $\sigma_{33}(0\phi) \simeq (1 + r_3)/2$.

Polarization

Treatment of Intermediate States

In the case of multiple intermediate levels, we can sum over states $|2\rangle$ to obtain the total polarization. According to energy of each intermediate state and its transition dipole moments, one can determine the fractional contribution of each state to the nonlinear index given in Eq. (7). However, treatment of multiple intermediate levels in the two-photon vector model shouldn't be important for comparing simulations with future experiments (except in the case when population redistribution is significant). This is because the additive contribution of each intermediate state to the nonlinear index $\sim \mu_{12}\mu_{23}/(\omega_{21} - \omega_0)$ is of the same form as its contribution to the more general expression for the nonlinear polarization, see Eq. (9) and

Eq. (5a), thereby producing a response that is representative of a two-photon-transition with only one intermediate state.

Two-Photon Absorption Rate

Solving Eq. (3) given the initial condition $r(t=0) = (0,0,-1)$ and a constant (or slowly varying in time) field amplitude and phase, i.e. , $\dot{\gamma}/\gamma^2 \ll 1$, we obtain $r_3 = -1 + \gamma_1^2\left(1-\cos\left(t\sqrt{\gamma_1^2+\Delta^2}\right)\right)\Big/(\gamma_1^2+\Delta^2)$. We can then express the two-photon excited population ρ_{33} as $\rho_{33} \approx (1+r_3)/2 = \gamma_1^2 \sin^2\left(t\sqrt{\gamma_1^2+\Delta^2}/2\right)\Big/(\gamma_1^2+\Delta^2) \sim 10^{-9}$ for the average field intensity and detuning given in Table 2. For long times, in the low-intensity limit, we express ρ_{33} as a function of frequency and obtain the following function which peaks at $\Delta = 0$: $\rho_{33}(\Delta) \approx \dfrac{\gamma_1^2 \sin^2(t\Delta/2)}{\Delta^2} = \dfrac{\pi\gamma_1^2 t}{2}\left[\dfrac{\sin^2(\Delta t/2)}{\pi(t/2)\Delta^2}\right]$. Applying the relation for the long time limit, we can recover the standard two-photon absorption rate $R_{2\gamma}$. The transition probability is given by $R_{2\gamma}t = \int\left[\lim_{(t/2)\to\infty}\rho_{33}(\Delta)\right] g(\Delta)\mathrm{d}\Delta = (\pi\gamma_1^2 t/2)\int\delta(\Delta)g(\Delta)\mathrm{d}\Delta$, from which we obtain: $R_{2\gamma} = \pi\gamma_1^2 g(0)/2 = 2\pi g(0)(\Omega_{12}\Omega_{23})^2/(\omega_{21}-\dot{\phi})^2$, where $g(\Delta)$ is the energy density. After 50m propagation according to the parameters in Table 2, the energy density on-resonance is given by $g(0) \sim 10^{-3}$ THz^{-1}. Hence a transition rate $R_{2\gamma} \sim$ kHz is obtained for a sufficiently slowly varying field amplitude and phase, i.e. $\dot{\gamma}/\gamma^2 \ll 1$.

Part IV

Remote Optical Magnetometry

Here we analyze a mechanism for remote optical measurements of magnetic field variations above the surface of seawater. This magnetometry mechanism is based on the polarization rotation of reflected polarized laser light, in the presence of the earth's magnetic field. Here the laser light is reflected off the surface of the water and off an underwater object. Two mechanisms responsible for the polarization rotation are the Surface Magneto-Optical Kerr Effect (SMOKE) and the Faraday effect. In both mechanisms the degree of polarization rotation is proportional to the earth's local magnetic field. Variations in the earth's magnetic field due to an underwater object will result in variations in the polarization rotation of the laser light reflected off the water's surface (SMOKE) and off the underwater object (Faraday effect). An analytical expression is obtained for the polarization-rotated field when the incident plane wave is at arbitrary angle and polarization with respect to the water's surface. We find that the polarization rotated field due to SMOKE is small compared to that due to the Faraday effect.

1 Introduction

Optical magnetometry can be a highly sensitive method for measuring small variations in magnetic fields [1-3]. The development of a remote optical magnetometry system can have important applications for the detection of underwater and underground objects that perturb

the local ambient magnetic field. For magnetic anomaly detection (MAD) applications, magnetic field variations must be detected at standoff distances greater than from the detector [4-5]. The remote atmospheric optical magnetometry mechanism considered here is based on polarization changes in reflected laser light from the sea water surface.

The dielectric properties of water in the presence of a magnetic field will cause the polarization of an optical field to rotate. The polarization rotation occurs via two distinct mechanisms: the Surface Magneto-Optical Kerr Effect (SMOKE) and the Faraday rotation effect. SMOKE is purely a surface phenomenon in which the degree of polarization rotation of the reflected light is proportional to the magnetic field and independent of the propagation distance in the dielectric medium [6]. The SMOKE mechanism is used in material science research, for example, the Kerr microscope. The Faraday effect is due to the difference in propagation speed of right-hand and left-hand polarized light, and the resulting degree of polarization rotation is proportional to both, the magnetic field and the propagation distance.

Here in Part III, we analyze whether these effects can be used for the remote detection of underwater objects. An underwater object can produce appreciable magnetic field perturbations above the water's surface. The analyzed magnetometry detection configuration is shown schematically in Fig. 18. Here, a linearly-polarized blue-green laser beam is propagated to and reflects off the water's surface near the detection site. The degree of polarization rotation in the reflected field is proportional to the local magnetic field. The magnitude of the polarization-rotated component of the reflected field is measured at various locations near the detection site. An irregularity in the measurement at one location would correspond to a variation in the local magnetic field. The local field variation indicate the presence of an

underwater object.

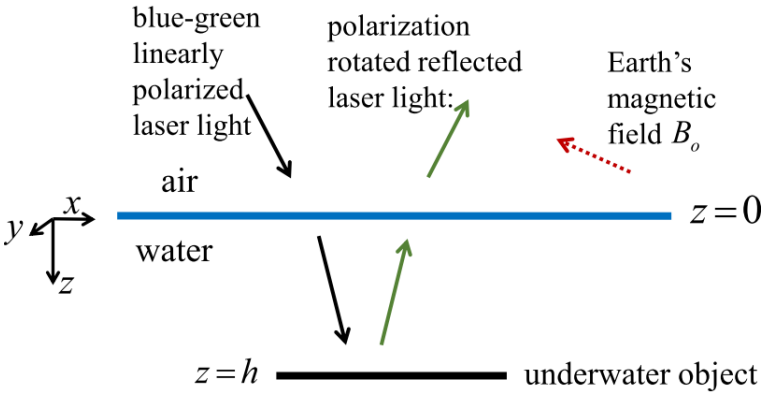

Figure 18: Polarized laser light is propagated to the surface of the water and exhibits polarization rotation upon reflection due to Faraday rotation and SMOKE. The solid arrows in the figure denote wave vectors.

The purpose is to estimate the degree of polarization rotation in the reflected field. If the polarization rotation is large enough, the mechanism schematically outlined in Fig. 18 may enable the measurement of variations in the earth's magnetic field. This may indicate the presence of an underwater object.

2 Model

To analyze the Surface Magneto-Optical Kerr and the Faraday rotation effects, we first obtain the dielectric properties of magnetized, pure water. The polarization field associated with magnetized water at the laser frequency is obtained using an extended form of the Lorentz model [7]. The polarization field is used to derive a wave equation for the reflected laser field. By appropriately matching boundary conditions at the various interfaces, we obtain the reflected field which has its polarization modified by both the SMOKE and Faraday effect. The polarization-rotated component of the field is proportional to the local magnetic field. In

applying the boundary conditions, the laser propagation direction and polarization as well as the Earth's magnetic field are taken to be in an arbitrary direction.

2.1 Polarization Field of Magnetized Water

In the Lorentz model, the dielectric properties of the molecule are represented by the motion of the forced displacement of the electron distribution from its equilibrium position. The displacement of the electron distribution $\delta\mathbf{r}(\mathbf{r},t)$ is modeled by the following driven harmonic oscillator equation,

$$\left(\frac{\partial^2}{\partial t^2} \; + \; \Omega_B^2 \; + \; \gamma\frac{\partial}{\partial t}\right)\delta\mathbf{r} \; = \; \frac{q}{m}\left(\mathbf{E} \; + \; \frac{\partial\delta\mathbf{r}}{\partial t} \; \times \; \mathbf{B}_o/c\right), \tag{1}$$

where Ω_B is the electron binding frequency, γ is the effective damping rate of water in the optical regime, q is the electronic charge, m is the electronic mass, and $\mathbf{B_o}$ is the local magnetic field, i.e., Earth's magnetic field $\sim$ 0.5G. The laser electric field is $\mathbf{E}(\mathbf{r},t) \; = \; \mathrm{Re}\left(\hat{\mathbf{E}}(\mathbf{r})\,\exp(-\,i\,\omega\,t)\right)$ whereω is the frequency. The magnetic field associated with the laser is neglected on the right hand side of Eq. (1) since it produces forces at frequencies of 2ω and 0.

The polarization field associated with the magnetized water molecules is given by $\hat{\mathbf{P}}\,(\mathbf{r}) = qN\delta\hat{\mathbf{r}}$, where $\delta\hat{\mathbf{r}}(\mathbf{r})$ represents the electronic displacement from equilibrium of the water molecule, $N$is the effective bound electron density of the water molecules, and phasor notation is used throughout to represent the various field quantities, i.e., $Q\,(\mathbf{r},t) \; = \; \mathrm{Re}\left(\hat{Q}\,(\mathbf{r})\exp\,(-\,i\,\omega\,t)\right)$.

The displacement $\delta\hat{r}(\mathbf{r})$ is given by

$$(-\omega^2 \;+\; \Omega_B^2 \;-\; i\,\gamma\,\omega)\,\delta\hat{\mathbf{r}}(\mathbf{r}) \;=\; q\left(\hat{\mathbf{E}}(\mathbf{r}) \;-\; i\,\omega\,\delta\hat{\mathbf{r}}(\mathbf{r})\times\mathbf{B}_o/c\right)/m. \tag{2}$$

The polarization field, correct to first order in the magnetic field, is

$$\hat{\mathbf{P}}\,(r) \;=\; q\,N\,\delta\hat{\mathbf{r}} \;\approx\; \frac{\omega_{pN}^2}{4\,\pi\,D\,(\omega)}\times\;\left(\hat{\mathbf{E}}(\mathbf{r}) \;+\; i\,\omega\;\Omega_o\times\hat{\mathbf{E}}(\mathbf{r})/D\,(\omega)\right), \tag{3}$$

where $D\,(\omega) \;=\; \Omega_B^2 \;-\; \omega^2 \;-\; i\,\gamma\,\omega$, $\omega_{pN} \;=\; (4\pi q^2 N/m)^{1/2}$, and $\Omega_0 = q\mathbf{B_o}/mc$ is the cyclotron frequency. The laser frequency is chosen to be in the blue-green range where the penetration depth is maximum. In the blue-green regime, the real part of the refractive index is $\mathrm{Re}[n_0] \approx 1.34$. In the following examples, the laser frequency is taken to be $\omega \;=\; 3.8\times10^{15}$rad/s ($\omega = 2.48\,\mathrm{eV}/\hbar$) where pure water's absorption coefficient is minimum, i.e., $\alpha \;=\; 5{\times}10^{-4}\mathrm{cm}^{-1}$; the corresponding penetration depth (e-folding length) is $h_e \;\approx\; 20\,\mathrm{m}$. The lowest energy electron-binding frequency in water is $\Omega_B \;\approx\; 23.5\mathrm{eV}/\hbar$, $\omega_{pN} \;\approx\; 21\mathrm{eV}/\hbar$, and the effective damping rate of water in the optical regime is $\gamma \;\approx\; 3\times10^9 s^{-1}$. The cyclotron frequency corresponding to $B_o \sim 0.5\,G$ is $\Omega_o \sim 10^7\,s^{-1}$.

In general, there are many resonances above Ω_B which contribute to the refractive index of water. We neglect these binding frequencies since they correspond to substantially higher energies and have little effect on the dielectric properties of water in the optical regime. In addition, the oscillator strength parameter associated with the Ω_B resonance is taken to be unity [8]. Nonlinear effects in water are neglected since the laser intensity is well below the level where these become important.

2.2 Wave Equation

In the absence of free charges and currents, Maxwell's equations for the fields in phasor notation are given by $\nabla \times \hat{\mathbf{H}} \;=\; -\,i\,(\omega/c)\,\hat{\mathbf{D}}$, $\nabla \cdot \hat{\mathbf{D}} \;=\; 0$, $\nabla \times \hat{\mathbf{E}} \;=\; i\,(\omega/c)\,\hat{\mathbf{B}}$, and $\nabla \cdot \hat{\mathbf{B}} \;=\; 0$. These equations can be combined to give

$$\nabla^2 \hat{\mathbf{E}} \;+\; (\omega^2/c^2)\,\hat{\mathbf{D}} \;=\; \nabla(\nabla \cdot \hat{\mathbf{E}}). \tag{4}$$

To obtain a wave equation for $\hat{\mathrm{E}}$, we note that the electric flux density $\hat{\mathbf{D}} = (\hat{\mathbf{E}} \;+\; 4\,\pi\,\hat{\mathbf{P}})$ is given by $\hat{\mathbf{D}} \;=\; (\varepsilon_o \;+\; i\,(\varepsilon_o \;-\; 1)\,(\omega/D(\omega))\,\mathbf{\Omega_o}\times\,)\;\hat{\mathbf{E}}$, where the electric polarization field is given in Eq. (3) and where the dielectric constant of water, in the absence of the earth's magnetic field, is $\varepsilon_o(\omega) \;=\; 1 \;+\; \omega_{PN}^2/D(\omega)$. Since $\nabla \cdot \hat{\mathbf{D}} \;=\; 0$, we find that

$$\begin{aligned} &\nabla \cdot \hat{\mathbf{E}} \;=\; -\,i\,\frac{(\varepsilon_o \;-\; 1)}{\varepsilon_o}\,\frac{\omega}{D(\omega)}\,\nabla \cdot\,(\mathbf{\Omega_o} \times \hat{\mathbf{E}}) \;= \\ &i\,\frac{(\varepsilon_o \;-\; 1)}{\varepsilon_o}\,\frac{\omega}{D(\omega)}\,(\mathbf{\Omega_o} \cdot (\nabla \times \hat{\mathbf{E}})), \end{aligned} \tag{5}$$

where the final form for $\nabla \cdot \hat{\mathbf{E}}$ is valid since $\mathbf{\Omega_o}$ is spatially uniform. Using Eqs. (4) and (5), the wave equation takes the form

$$\begin{aligned} &\nabla^2 \hat{\mathbf{E}} \;+\; \varepsilon_o\,\frac{\omega^2}{c^2}\,\hat{\mathrm{E}} \;=\; -\,i\,\frac{\omega^2}{c^2}(\varepsilon_o \;-\; 1)\,\frac{\omega}{D(\omega)}\,(\mathbf{\Omega_o} \times \hat{\mathbf{E}}) \\ &+\; i\,\frac{(\varepsilon_o \;-\; 1)}{\varepsilon_o}\,\frac{\omega}{D(\omega)}\,\nabla(\mathbf{\Omega_o} \cdot (\nabla \times \hat{\mathbf{E}})). \end{aligned} \tag{6}$$

The right-hand side of Eq. (6) can be simplified by noting that $\nabla(\mathbf{\Omega_o} \cdot (\nabla \times \hat{\mathbf{E}})) \;=\; \mathbf{\Omega_o} \times (\nabla \times \nabla \times \hat{\mathbf{E}})) \;+\; (\mathbf{\Omega_o} \cdot \nabla)(\nabla \times \hat{\mathbf{E}})$ and, to lowest order in $\mathbf{\Omega_o}$, $\nabla \times \nabla \times \hat{\mathbf{E}} \;=\; (\omega^2/c^2)\varepsilon_o\hat{\mathbf{E}}$.

The final form for the wave equation, correct to first order in $\mathbf{\Omega_o}$, is

$$\left(\nabla^2 \; + \; \varepsilon_o \frac{\omega^2}{c^2}\right) \hat{\mathrm{E}} \; = \; i \, \frac{(\varepsilon_o \, - \, 1)}{\varepsilon_o} \, \frac{\omega}{D(\omega)} \, (\mathbf{\Omega_o} \cdot \nabla)(\nabla \times \hat{\mathbf{E}}). \tag{7}$$

Since the right-hand side of Eq. (7) is small, we can write the total field as $\hat{\mathbf{E}}(\mathbf{r}) \; = \; \hat{\mathbf{E}}_o \; + \; \delta\hat{\mathbf{E}}$, where $\hat{\mathbf{E}}_o$ here denotes the laser field in the absence of the perturbation (i.e. the Earth's magnetic field) and $\delta\hat{\mathbf{E}}$ is the small polarization-modified component of the laser field due to the Earth's magnetic field and induced by the laser field $\hat{\mathbf{E}}_o$. Separate wave equations can be written for these fields:

$$\left(\nabla^2 \; + \; \varepsilon_o \frac{\omega^2}{c^2}\right) \hat{\mathrm{E}}_o \; = \; 0, \tag{8a}$$

$$\left(\nabla^2 \; + \; \varepsilon_o \frac{\omega^2}{c^2}\right) \delta\hat{\mathrm{E}} \; = \; i \, \frac{(\varepsilon_o \, - \, 1)}{\varepsilon_o} \, \frac{\omega}{D(\omega)} \, (\mathbf{\Omega_o} \cdot \nabla)(\nabla \times \hat{\mathbf{E}}_o). \tag{8b}$$

In the special case where the laser field $\mathbf{E}_o$ is transverse to the magnetic field $\mathbf{B}_o$, one can recover from Eq. (8b) the usual Faraday rotation angle, i.e. $\Delta\theta_F \; \approx \; \omega_{pN}^2 \, \omega^2 \, \Omega_0 \, L/(2\, c \, \Omega_B^4) \; \sim \; (10^{-4} \; \mathrm{G^{-1}m^{-1}rad}) L \, B_o$, where L is the propagation distance [9]. These wave equations, Eq. (8a,b), are numerically solved for arbitrary laser field propagation direction, polarization and magnetic field direction.

3 Polarization Rotation

The magnetometry method is based on the polarization rotation of reflected laser radiation. The reflection occurs both off the surface of the water (SMOKE effect) and off the underwater object (Faraday effect). The purpose of the analysis is thus to calculate the degree of polarization rotation as denoted by $\Delta\theta = (1/R)|\delta E|/|E_0|$, where δE is the polarization-rotated component of the reflected laser field, E_0 is the incident laser field and the reflection coefficient is $R = (n_o - 1)/(n_o + 1) \approx 0.15$.

We first consider a simplified configuration as shown in Fig. 19 to obtain estimates for the amount of polarization rotation, i.e., $\Delta\theta$. In this simplified configuration, a linearly-polarized, monochromatic laser beam is propagated parallel to Earth's magnetic field which is taken to be perpendicular to the surface of the water. An optically reflective underwater object at depth h below the water's surface is represented by a perfectly conducting plate parallel to the surface. Two distinct contributions will emerge from this simplified configuration to the polarization rotation, i.e., the Faraday effect and SMOKE.

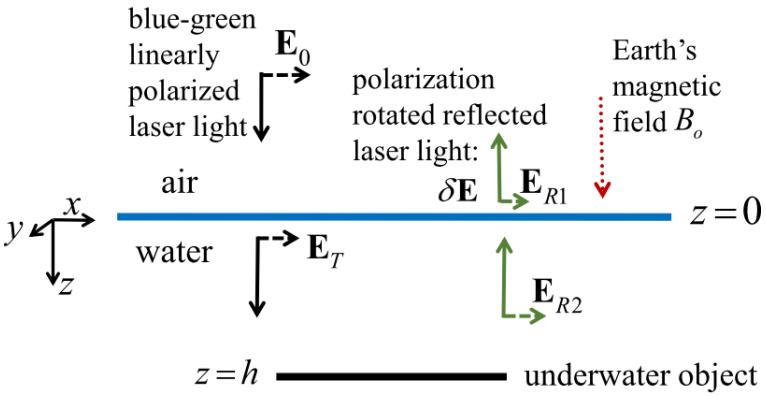

Figure 19: A simplified configuration of reflected laser light undergoing polarization rotation due to Faraday rotation and SMOKE. The purpose of this configuration is to obtain estimates for the polarization rotation angle $\Delta\theta$.

The solid arrows in Fig. 19 represent the wave vectors while the dashed arrows denote the electric fields corresponding to the incident wave $\mathbf{E}_o$, the transmitted wave $\mathbf{E}_T$, the object-reflected wave $\mathbf{E}_{R2}$, and the surface-reflected wave $\mathbf{E}_{R1}$ which is modified by a small polarization-rotated component $\delta\mathbf{E}$. The electric field for z < 0 (air) can be written as,

$$\hat{\mathbf{E}}(z) \;=\; \mathrm{E}_0 \exp(ikz)\hat{e}_x \;+\; \mathrm{E}_{\mathrm{R1}} \exp(-ikz)\hat{e}_x + \delta\mathrm{E} \exp(-ikz)\hat{e}_y, \tag{9a}$$

and for 0 < z < h (water),

$$\hat{\mathbf{E}}(z) \;=\; \mathrm{E}_{\mathrm{T}}^{+} \exp(ik_{+}z)\hat{e}_{+} \;+\; \mathrm{E}_{\mathrm{T}}^{-} \exp(ik_{-}z)\hat{e}_{-} \;+ \mathrm{E}_{\mathrm{R2}}^{+} \exp(-ik_{+}z)\hat{e}_{+} \;+\; \mathrm{E}_{\mathrm{R2}}^{-} \exp(-ik_{-}z)\hat{e}_{-}, \tag{9b}$$

where $\hat{e}_{\pm} \;=\; (\hat{e}_x \;\pm\; i\,\hat{e}_y)/\sqrt{2}$, $\hat{e}_x$and $\hat{e}_y$ are unit vectors in the x and y direction respectively, $k = \omega/c$ is the wavenumber in air, $n_{\pm} \;=\; ck_{\pm}/\omega \;=\; \sqrt{\varepsilon_o \;\pm\; \varepsilon_1}$ is the complex index of refraction in magnetized water, and $\varepsilon_1 \;=\; (\varepsilon_o \;-\; 1)\,\omega\,\Omega/D(\omega)$. Application of the electromagnetic boundary conditions yields for the configuration shown in Fig. 19 the following ratio for the polarization-rotated field,

$$\frac{\delta E}{E_0} \;=\; -i \left(\frac{n_{+} \cos\left(k_{+}h\right)}{n_{+} \cos\left(k_{+}h\right) \;-\; i \sin\left(k_{+}h\right)} \;-\; \frac{n_{-} \cos\left(k_{-}h\right)}{n_{-} \cos\left(k_{-}h\right) \;-\; i \sin\left(k_{-}h\right)} \right) \;, \tag{10}$$

where $n_{\pm} \;\approx\; n_o\,(1 \;\pm\; (n_o^2 \;-\; 1)\omega\,\Omega_o/(2\,n_o^2 D(\omega)))$ is the refracted index corresponding to right and left-handed polarized waves. In the limit that $h \to \infty$, the reflected Faraday rotation vanishes and the polarization rotation is due solely to SMOKE. In the SMOKE limit Eq. (10)

reduces to

$$|\delta E/E_0|_{h\to\infty} \;=\; \frac{n_+ \,-\, n_-}{(1 \,+\, n_+)\,(1 \,+\, n_-)} \;=\; \xi, \tag{11}$$

where $\xi \;\approx\; (n_0 \,-\, 1)(\omega\,\Omega_0/\Omega_B^2)/(n_0^2 \,+\, n_0) \;\sim\; 3\times 10^{-12}$. The ratio of the fields given in Eq. (10) is shown in Fig. 20 as a function of the depth of the conducting plate h.

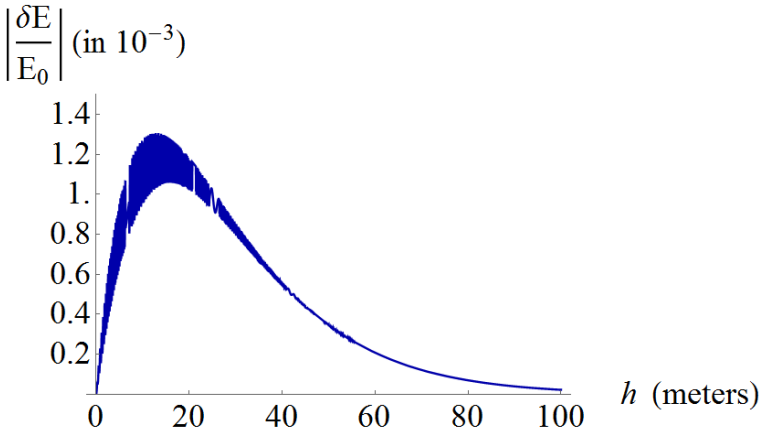

Figure 20: Ratio of the polarization-rotated reflected field to the incident field as a function of object depth h, according to Eq. (10). The polarization rotation results from a combination of Faraday rotation and SMOKE; however, the contribution due to SMOKE is small.

The Faraday effect yields the ratio $|\delta E/E_0| \;\sim\; 12\,\pi\,n_0\,h\,\xi/\lambda$, whereas SMOKE yields $|\delta E/E_0| \approx \xi \sim 3\times 10^{-12}$. The Faraday effect is larger by the ratio $h/\lambda \gg 1$.

We now consider the general SMOKE contribution to the polarization rotation by analyzing the process for arbitrary field directions. The polarization-rotated field due to SMOKE as a function of the field components of an incident plane wave, for arbitrary polarizations and angle of incidence as well as arbitrary orientation of the magnetic field, is obtained in the Supplement. The general expression for the rotated polarization component of the field is

$$\delta E_{R,\perp} = \frac{-i\mathrm{K}\beta(E_x, E_y, \theta, \theta_B, \phi_B)}{\sqrt{|E_x|^2 + P^2|E_y|^2}}\ , \tag{12}$$

where $\mathrm{K} = \Omega_0\omega(n_R-1)/\Omega_B^2 n_R(n_R+1) \sim 2.5\times10^{-12}$, $\beta = \cos\theta_B(u_1|E_x|^2 + u_2P|E_y|^2) + \sin\theta_B\cos\phi_B(u_3E_xE_y^*) + \sin\theta_B\sin\phi_B(u_4|E_x|^2 + u_5P|E_y|^2)$, and $P(\theta), u_i(\theta) \sim 1$. In Eq. (12), E_x and E_y are the components of the incident field, and θ is the angle of the incident wave vector with respect to the water's surface normal vector. The angles θ_B and ϕ_B are, respectively, the polar and azimuthal angle of Earth's magnetic field with respect to the incident wave vector, see Supplement.

Equation (12) is written with the explicit θ dependence the Supplement, see Eq. (15). The angular function $u_1(\theta)$ is used to construct the following plot of SMOKE's angular dependence, for which the local magnetic field is taken to be parallel to the incident wave vector i.e. $\theta_B = \phi_B = 0$, $\mathrm{E}_y = 0$.

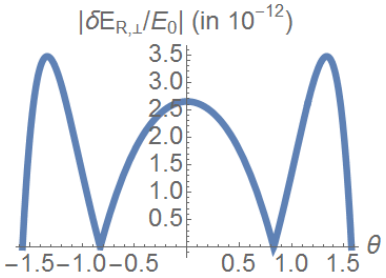

Figure 21: $n_R = 1.34$.

Figure 22: The function $|\delta E_{R,\perp}/E_0|$ plotted above represents the dependence of the polarization-rotated field on the incident wave vector's orientation for a specific geometry ($\theta_B = 0, \mathrm{E}_y = 0$), according to Eq. (15). Here $\delta E_{R,\perp}$ is the polarization-rotated component of the reflected laser field and E_0 is the incident laser field. This plot is specific to water with refractive index $n_R = 1.34$.

The angular dependence of Eq. (12) is further analyzed in the Supplement, where it is shown that an alternative geometry can increase $|\delta E_{R,\perp}/E_0|$ to 5.1×10^{-12}. We find, however, that no choice of polarization or angle of incidence will significantly increase the SMOKE contribution to the polarization rotation, see Fig. 21. The SMOKE contribution thus is too small to serve as a feasible mechanism for the measurement of the local magnetic field or for

the measurement of small variations in this field.

Regarding the Faraday effect contribution, small variations in the magnetic field are not of interest. Even so, measurement of the field ratio, $|\delta E/E_0| \sim \ 12\,\pi\,n_0\,h\,\xi/\lambda \sim 10^{-3}$ (see Fig. 20), may be complicated by a number of factors which we address in the remainder of this section.

The underwater object's surface may not be conducting; in the case of rubber ($n_R = 1.52$), we find that 98% of the energy is lost to transmission, which would require $|\delta E/E_0| \sim 10^{-4}$. Alternatively, the object may not be in the desired depth range; a sub-meter or above-80m depth will require $|\delta E/E_0| < 10^{-4}$, see Fig. 20.

With regard to variations in temperature, even if the laser beam propagates through water that is fairly hot, the Faraday contribution will be increased by only a small amount, according to $|\delta E/E_0| \ \propto (n_0(T)-1)/\Omega_B^2(n_0(T)+1)$, where the change in the parameter Ω_B^2 with respect to temperature yields, approximately, $|\delta E/E_0| \ \propto (n_0(T)-1)^2/(n_0(T)+1)^2$.

Regarding orientations in space, a percentage of the signal will be lost if the laser beam's path somewhat bypasses the underwater object or if the object's geometry is such that it mostly reflects the beam away from the detector's surface. A non-vertical magnetic field at angle θ with respect to the water's surface will reduce the signal by a factor of $\sec\theta$.

At the water's surface, bubbles and ripples on a smaller spatial scale than the laser beam radius will likely refract away a significant amount of the available signal, and waves on a larger spatial scale than the laser beam radius may refract away the full signal, requiring multiple measurement attempts in each location.

4 Discussion

We have analyzed mechanisms for the possible remote optical measurement of magnetic field variations above the surface of seawater. In this process, a polarized blue-green laser beam is reflected off the water's surface and the reflected, polarization-rotated electric field recorded. A variation in the measurements at nearby locations may indicate the presence of an underwater conducting object. The two mechanisms responsible for the polarization rotation are the Surface Magneto-Optical Kerr Effect (SMOKE) and the Faraday effect. An analytical expression is obtained for the polarization-rotated field when the incident plane wave is at arbitrary angle and polarization with respect to the water's surface. We conclude that the polarization rotated field due to SMOKE is small and would challenging to implement as a magnetometry mechanism. The Faraday effect is feasible for shallow ($\sim$ 1-10 m) conducting objects. Such an object would be too light to detect via gravitational field measurements, and though sonar is a viable detection method, it is a more local method.

Underwater objects may be detected directly by measuring the un-rotated component of the reflected laser field. By time gating the incident laser pulses and measuring the total reflected field, the object's depth can be determined.

5 References

[1] D. Budker, W. Gawlik, D.F. Kimball, S.M. Rochwester, V.V. Yashchuk and A. Weis, Rev. Mod. Phys. 74, 1154 (2002).

[2] Optical Magnetometry, D. Budker and D.F.J. Kimball (eds.) (Cambridge University Press,

Cambridge, UK, 2013).

[3] G. Bison, R. Wynands, and A. Weis, Appl. Phys. B Lasers Opt. 76, 325 (2003).

[4] J.P. Davis, M.B. Rankin, L.C. Bobb, C. Giranda, M.J. Squicciarini, "REMAS Source Book," Mission and Avionics Tech. Dept., Naval Air Development Center (1989).

[5] L. A. Johnson, P. Sprangle, B. Hafizi, and A. Ting. "Remote atmospheric optical magnetometry," Journal of Applied Physics, 116(6), (2014).

[6] Z. Qiu and S. Bader, "Surface magneto-optical Kerr effect," Review of Scientific Instruments 71 (3), 1243-1255 (2000).

[7] K. Oughstun and R. Albanese, "Magnetic field contribution to the Lorentz model," J. Opt. Soc. Am. A 23, 1751-1756 (2006).

[8] J. D. Jackson, Classi cal electrodynamics. (Wiley, New York, 1999).

[9] Andrei, E. 2015. Faraday Rotation [pdf]. Retrieved from:
http://www.physics.rutgers.edu/grad/506

6 Supplement

A perturbative analysis on the wave equations in Eqs.(8a,b) is performed to obtain the polarization rotated reflected field associated with SMOKE. The treatment allows for the incident field to have an arbitrary angle and polarization with respect to the water's surface and allows for arbitrary magnetic field orientation. The coordinate system used in this analysis is shown in Fig. 23.

The incident wave vector is denoted by the arrow in the $z' < 0$ (air) regime; its direction defines the z axis. The plane's normal vector to the water's surface plane defines the z' axis.

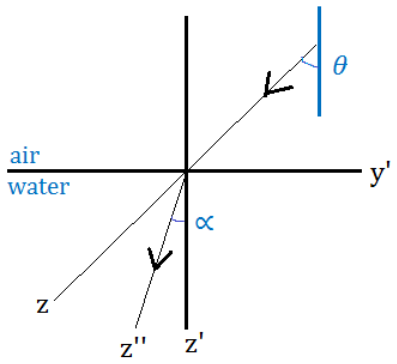

Figure 23: Coordinate systems used in the calculation of the polarization-rotated reflected field associated with SMOKE for an arbitrary geometric configuration.

The arrow in the water region corresponds to the transmitted wave vector in the absence of a magnetic field. The boundary conditions ensure that it is coplanar with the z and z' axis and that $k_0 \sin\alpha = (\omega/c)\sin\theta$, where k_0 is the magnitude of the transmitted wave vector. The coordinate systems are defined such that $x = x' = x''$ coincide.

The fields $\hat{E}(\mathbf{r})$, $\hat{D}(\mathbf{r})$, and $\hat{B}(\mathbf{r})$ are expanded to first order in the small parameter $\Delta = \omega\,\Omega_0/D(\omega) \sim 10^{-11}$. The field is written in the form $\hat{E}(\mathbf{r}) = \hat{E}_0(\mathbf{r}) + \delta\hat{E}(\mathbf{r})$, where $\mathbf{E}_0$ is the field in the absence of a magnetic field and $\delta\hat{E}(\mathbf{r})$ is the first order correction to the field due to the magnetic field. The wave equations for $\mathbf{E}_0$ and $\delta\mathbf{E}$ have been derived, i.e. Eq. (8a,b), and are repeated below for convenience,

$$\left(\nabla^2 + \varepsilon_o \frac{\omega^2}{c^2}\right)\hat{\mathrm{E}}_o = 0 \tag{13a}$$

$$\left(\nabla^2 + \varepsilon_o \frac{\omega^2}{c^2}\right)\delta\hat{\mathrm{E}} = i\,\frac{(\varepsilon_o - 1)}{\varepsilon_o}\,\frac{\omega}{D(\omega)}\,(\mathbf{\Omega_o}\cdot\nabla)(\nabla\times\hat{\mathbf{E}}_o) \tag{13b}$$

The fields can be written in the form

$$\delta\hat{E}(\mathbf{r}) \;=\; \delta\hat{A}(\mathbf{r})\exp(ik_0 z'') \text{ and } \hat{E}_0(\mathbf{r}) \;=\; A_{T,0}\exp(ik_0 z''),$$

in order to employ the paraxial approximation,$\nabla^2 \;\rightarrow\; -\,{k_0}^2 \;+\; 2ik_0\partial/\partial z''$, which implies that the field varies little over a wavelength. Applying the paraxial approximation to Eq. (13b) yields

$$\partial\delta\hat{A}(\mathbf{r})\,/\partial z'' = \frac{i\,(\varepsilon_0 \;-\; 1)\,\omega\,(\Omega_0 \cdot ik_0\hat{\mathbf{z}}'')\,(i\,k_0\widehat{\mathbf{z}}'' \times A_{T,0})}{2\,i\,k_0\,\varepsilon_0\,D(\omega)}, \tag{14}$$

where $z' \;>\; 0$ (water). The right-hand side of Eq. (14) is independent of spatial variables and yields $\delta\hat{A}(\mathbf{r}) \;=\; a \;+\; z'b$, where $b = \dfrac{i\,(\varepsilon_0 \;-\; 1)\,\omega\,(\Omega_0 \cdot ik_0\hat{\mathbf{z}}'')\,(ik_0\hat{\mathbf{z}}'' \times A_{T,0})}{2ik_0\varepsilon_0 D(\omega)\cos\alpha}$. We have used the fact that the boundary conditions equate the spatial dependence of $\delta\hat{A}(\mathbf{r})$ and $\nabla \times \delta\hat{A}(\mathbf{r})$ at $z' = 0$. Having solved the wave equation in each regime, we now apply the boundary conditions. The electric field boundary conditions allow us to express a in terms of the components of $\delta\hat{E}_R$ which denotes the first order correction to the reflected field $\hat{E}_R$. Three linearly independent equations for $\delta\hat{E}_R$ are obtained by equating the tangential magnetic fields at the boundary. Solving these equations yields a complicated expression for $\delta\hat{E}_R$. This expression is not, in general, perpendicular to the zeroth order reflected field. Thus, the desired expression for the polarization rotated field $\delta E_{R,\perp}$ is given by

$$\delta E_{R,\perp} = \delta\hat{E}_R \cdot (\hat{\mathbf{z}}_{\text{ref}} \times \hat{E}_{0,R})^* \Big/ |\hat{E}_{0,R}|,$$

where $\hat{E}_{0,R}$ is the zeroth order reflected field at $z' = 0$ and $\hat{\mathbf{z}}_{ref}$ is the direction along which it

propagates. The polarization rotated field $\delta E_{R,\perp}$ is given by

$$\delta E_{R,\perp} = \frac{-i\mathrm{K}\beta(E_x, E_y, \theta, \theta_B, \phi_B)}{\sqrt{|E_x|^2 + P^2|E_y|^2}} \ , \tag{15}$$

where $\mathrm{K} = \Omega_0\omega(n_R - 1)/\Omega_B^2 n_R(n_R + 1) \sim 2.5 \times 10^{-12}$ and

$$\beta = \cos\theta_B(u_1|E_x|^2 + u_2 P|E_y|^2) + \sin\theta_B\cos\phi_B(u_3 E_x E_y^*) + \sin\theta_B\sin\phi_B(u_4|E_x|^2 + u_5 P|E_y|^2). \cdot$$

The angular functions P and u_i are given by:

$$P(\theta) = \frac{\left(\cos\theta + \sqrt{n_R^2 - \sin^2\theta}\right)\left(\sin^2\theta + n_R^2\left(-1 + \cos\theta\sqrt{n_R^2 - \sin^2\theta}\right)\right)}{\left(\cos\theta - \sqrt{n_R^2 - \sin^2\theta}\right)\left(-\sin^2\theta + n_R^2\left(1 + \cos\theta\sqrt{n_R^2 - \sin^2\theta}\right)\right)} \ ,$$

$$u_i(\theta) = v_i(\theta)(n_R + 1)^2\cos\theta,$$

$$v_1(\theta) = -\frac{\cos\theta\left(n_R^2 - \sin^2\theta\right) + \sin^2\theta\left(-2n_R + \sqrt{n_R^2 - \sin^2\theta}\right)}{\left(\cos\theta + \sqrt{n_R^2 - \sin^2\theta}\right)\left(-\sin^2\theta + n_R^2\left(1 + \cos\theta\sqrt{n_R^2 - \sin^2\theta}\right)\right)} \ ,$$

$$v_2(\theta) = \frac{\sin^2\theta + \cos\theta\sqrt{n_R^2 - \sin^2\theta}}{\left(\cos\theta + \sqrt{n_R^2 - \sin^2\theta}\right)\left(n_R^2\cos\theta + \sqrt{n_R^2 - \sin^2\theta}\right)} \ ,$$

$$v_3(\theta) = -\frac{2n_R\sin\theta}{n_R^2 + n_R^4\cos^2\theta - \sin^2\theta + 2n_R^2\cos\theta\sqrt{n_R^2 - \sin^2\theta}} \ ,$$

$$v_4(\theta) = \frac{\sin\theta\left(n_R^2 - \sin^2\theta - \cos\theta\left(-2n_R + \sqrt{n_R^2 - \sin^2\theta}\right)\right)}{\left(\cos\theta + \sqrt{n_R^2 - \sin^2\theta}\right)\left(-\sin^2\theta + n_R^2\left(1 + \cos\theta\sqrt{n_R^2 - \sin^2\theta}\right)\right)} \ ,$$

$$v_5(\theta) = \frac{\sin\theta\left(\cos\theta - \sqrt{n_R^2 - \sin^2\theta}\right)}{\left(\cos\theta + \sqrt{n_R^2 - \sin^2\theta}\right)\left(n_R^2\cos\theta + \sqrt{n_R^2 - \sin^2\theta}\right)} \ .$$

In Eq. (15), θ is the angle of the incident wave vector with respect to the water's surface normal vector. The angles θ_B and ϕ_B are, respectively, the polar and azimuthal angle of

earth's magnetic field with respect to the incident wave vector where $\theta_B = \pi/2$, $\phi_B = 0$, corresponds to an orientation along the x axis (Fig. 23). The fields E_x and E_y correspond to the component of the incident electric field $\hat{E}(\mathbf{r})$ along the x and y axis, respectively. The angular functions used in this result are plotted in Fig. 24.

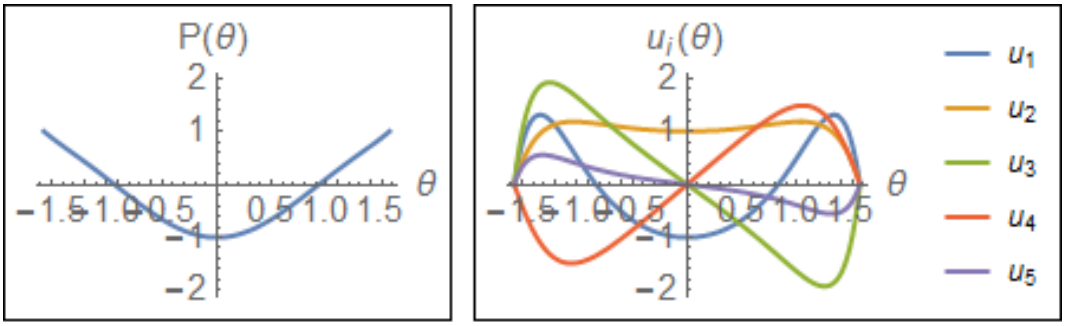

Figure 24: The functions above, within the context of Eq. (15), describe the angular dependence of the polarization-rotated field on the incident wave vector's orientation.

In the first plot of Fig. 24, the zero in $P(\theta)$ corresponds to the Brewster angle. From this plot, we see that $|P(\theta)| \leq 1$, which we will see is useful in minimizing the denominator of Eq. (15) and maximizing the amount of polarization rotation. From the second plot of Fig. 24, we see that when the incident wave propagates perpendicularly to the water's surface (as in the case of Fig. 19), i.e. , $\theta = 0$, the SMOKE contribution is proportional to the magnetic field component in the direction of propagation. The geometry of Fig. 19 is not optimal. The SMOKE contribution for water is largest when all of the following apply: i) the incident light comes in at the Brewster's angle (with respect to the water's surface normal vector), ii) the electric field of the incident wave is almost entirely polarized in the plane which contains the incident wave vector, the transmitted wave vector, and the water's surface normal vector, i.e. $0 < |E_x| \ll |E_y|$, and iii) the earth's magnetic field is perpendicular to this plane, i.e. $\theta_B = \pi/2, \phi_B = 0$. This specific geometry increases the polarization rotation by a factor of

$\approx$ 2 (corresponding to the peak of u_3 in Fig. 24) with respect to the geometry of Fig. 19. We find, however, that no choice of polarization or angle of incidence will significantly increase the SMOKE contribution to the polarization rotation.

Part V

List of Publications and Presentations

Publications:

[1] Epstein, Z., Lehmberg, R., and Sprangle, P., 2019. "Spectral Broadening of the NIKE KrF Laser via Propagation through Xenon in the Negative Nonlinear Index Regime." (Manuscript to be submitted April 2019).

[2] Epstein, Z., Hafizi, B., Peñano, J. and Sprangle, P., 2018. Generation of high-average-power ultra-broadband infrared radiation. JOSA B, 35(11), pp.2718-2726.

[3] Epstein, Z., Hafizi, B., Peñano, J. and Sprangle, P., 2018, May. High-average power, ultra-broadband, infrared radiation generation. In Ultrafast Bandgap Photonics III (Vol. 10638, p. 106381V). International Society for Optics and Photonics.

[4] Epstein, Z. and Sprangle, P., 2016. An Optical Magnetometry Mechanism Above the Surface of Seawater. IEEE Journal of Quantum Electronics, 52(6), pp.1-6.

Presentations:

[3] Epstein, Z., Hafizi B., Penano J., Sprangle P. "High Power Supercontinuum IR Generation." Invited Talk. Defense and Commerical Sensing, SPIE, Orlando, FL, Apr. 18, 2018.

[2] Epstein, Z., Sprangle, P., Penano, J. "High Power Supercontinuum Generation in the Atmospheric IR Window." Division Seminar. Plasma Physics Division (Code 6700), Naval Research Laboratory, Washington, DC, Oct. 13, 2016.

[3] Epstein, Z., Sprangle, P., Penano, J. "Generation of an IR-CM source using CO2 Beams." Directed Energy Scholar's Summer Intern Presentation, Naval Research Laboratory, Washington, DC, Sep. 12, 2016.

[4] Epstein, Z., Sprangle, P., Penano, J. "Generation of an IR-CM source using CO2 Beams." Directed Energy Scholar's Summer Kickoff, Naval Research Laboratory, Washington, DC, Jun. 10, 2016.

[5] Epstein, Z., Sprangle, P., Lehmberg, R. "Effect of the Delayed Nonlinear Response on Propagation of NIKE Laser through Xenon." Laser Plasma Branch (Code 6730), Naval Research Laboratory, Washington, DC, May 12, 2016.

[6] Epstein, Z., Sprangle, P. "Maximization of PV Cell Efficiency for the Remote Recharging of a UAV." Beam Physics Branch (Code 6790), Naval Research Laboratory, Washington, DC, Aug. 31, 2015.

[7] Epstein, Z., Sprangle, P., Ting, A. "Propagation of a 'Budding Flat-top' beam through Atmospheric Turbulence." Directed Energy Scholar's Summer Intern Presentation, Naval Research Laboratory, Washington, DC, Aug. 19, 2015.

[8] Epstein, Z., Sprangle, P., Ting, A. "Propagation through Atmospheric Turbulence." Directed Energy Scholar's Summer Kickoff, Naval Research Laboratory, Washington, DC, Jun. 19, 2015.

[9] Epstein, Z., Sprangle, P. "Optical Magnetometry Above the Surface of Seawater." Naval Engineering Education Center's Annual Meeting, Carderock, VA, Apr. 07, 2015. Poster.

[10] Epstein, Z., Sprangle, P."Remote Optical Magnetometry." IREAP Graduate Student Seminar, University of Maryland, College Park, MD, Mar. 13, 2015.

[11] Epstein, Z., Sprangle, P. "Optical Magnetometry Above the Surface of Seawater." American Society of Naval Engineers Day, Arlington, VA, Mar. 05, 2015. Poster.

[12] Epstein, Z., Johnson, L., Sprangle. P. "Laser Remote Sensing of Magnetic Fields in the Atmosphere by Optical Pumping Techniques," IREAP Laser-Matter Interactions Group Meeting, College Park, MD, Aug. 06, 2014.

Part VI
Complete Reference List

[II.1] Corkum, P.B., Ho, P.P., Alfano, R.R. and Manassah, J.T., 1985. Generation of infrared supercontinuum covering 3–14 μm in dielectrics and semiconductors. Optics letters, 10(12), pp.624-626.
[II.2] Pigeon, J. J., S. Ya Tochitsky, C. Gong, and C. Joshi. "Supercontinuum generation from 2 to 20 μm in GaAs pumped by picosecond CO 2 laser pulses." Optics letters 39, no. 11 (2014): 3246-3249.
[II.3] Pigeon, J.J., Tochitsky, S.Y. and Joshi, C., 2015. High-power, mid-infrared, picosecond pulses generated by compression of a CO 2 laser beat-wave in GaAs. Optics letters, 40(24), pp.5730-5733.
[II.4] Pigeon, J., Tochitsky, S. and Joshi, C., 2016, March. Generation of broadband 10 μm pulses using four-wave mixing compression in GaAs. In Mid-Infrared Coherent Sources (pp. MT2C-7). Optical Society of America.
[II.5] Kapetanakos, C.A., Hafizi, B., Milchberg, H.M., Sprangle, P., Hubbard, R.F. and Ting, A., 1999. Generation of high-average-power ultrabroad-band infrared pulses. IEEE journal of quantum electronics, 35(4), pp.565-576.
[II.6] Kapetanakos, C.A., Hafizi, B., Sprangle, P., Hubbard, R.F. and Ting, A., 2001. Progress in the development of a high average power ultra-broadband infrared radiation source. IEEE journal of quantum electronics, 37(5), pp.641-652
[II.7] Dudley, J.M., Genty, G. and Coen, S., 2006. Supercontinuum generation in photonic crystal fiber. Reviews of modern physics, 78(4), p.1135.
[II.8] Kolesik, M., Moloney, J.V. and Mlejnek, M., 2002. Unidirectional optical pulse propagation equation. Physical review letters, 89(28), p.283902.
[II.9] Kolesik, M. and Moloney, J.V., 2004. Nonlinear optical pulse propagation simulation: From Maxwell's to unidirectional equations. Physical Review E, 70(3), p.036604.
[II.10] Andreasen, J., and M. Kolesik. "Nonlinear propagation of light in structured media: Generalized unidirectional pulse propagation equations." Physical Review E 86, no. 3 (2012): 036706.
[II.11] Esarey, E., Sprangle, P., Krall, J. and Ting, A., 1997. Self-focusing and guiding of short laser pulses in ionizing gases and plasmas. IEEE Journal of Quantum Electronics, 33(11), pp.1879-1914.
[II.12] Sprangle, P., Penano, J.R. and Hafizi, B., 2002. Propagation of intense short laser pulses in the atmosphere. Physical Review E, 66(4), p.046418.
[II.13] Duarte, F.J., 1986. Variable linewidth high-power TEA CO2 laser." Applied optics 24(1), pp. 34-37.
[II.14] Frosz, M.H., 2010. Validation of input-noise model for simulations of supercontinuum generation and rogue waves. Optics express, 18(14), pp.14778-14787.
[II.15] Schubert, M., K-E. Susse, W. Vogel, and D-G. Welsch. "Influence of fluctuations of a laser pump on the intensity correlation of resonance fluorescence radiation." Optical and Quantum Electronics 12, no. 1 (1980): 65-76.
[II.16] Marshall, W.K., Crosignani, B. and Yariv, A., 2000. Laser phase noise to intensity

noise conversion by lowest-order group-velocity dispersion in optical fiber: exact theory. Optics letters, 25(3), pp.165-167.
[II.17] Isaacs, J. Sprangle, P., "The Effect of Laser Noise on the Propagation of Laser Radiation in Dispersive and Nonlinear Media," Proc. SPIE, Submitted.
[II.18] Nelson, W., Sprangle, P. and Davis, C.C., 2016. Atmospheric propagation and combining of high-power lasers. Applied optics, 55(7), pp.1757-1764.
[II.19] "Chalcogenide Glass Fibers." IRFlex Corporation. Accessed March 19, 2018. https://www.irflex.com s-series/.
[II.20] A. J. DeMaria and T. V. Hennessey, SPIE Professional Magazine, 50th Anniversary of Laser Devices (2010).
[II.21] Agrawal, G. (2013). Nonlinear fiber optics. 5th ed. Academic Press.
[II.22] WD Johnston, J.R. and Kaminow, I.P., 1969. Contributions to optical nonlinearity in GaAs as determined from Raman scattering efficiencies. Physical Review, 188(3), p.1209.
[II.23] Wood, R.M., Sharma, S.K. and Waite, P., 1983, June. Review of laser induced damage thresholds. In The Max Born Centenary Conference (pp. 84-87). International Society for Optics and Photonics.
[II.24] Wood, R.M., 2003. Laser-induced damage of optical materials. CRC Press.
[II.25] Cu/Ni/Au Mirrors. Retrieved January 1, 2017, from http://www.haaslti.com/copper-mirror-laser.html
[III.1] Obenschain, S., Lehmberg, R., Kehne, D., Hegeler, F., Wolford, M., Sethian, J., Weaver, J. and Karasik, M., 2015. High-energy krypton fluoride lasers for inertial fusion. Applied optics, 54(31), pp.F103-F122.
[III.2] Weaver, J., Lehmberg, R., Obenschain, S., Kehne, D. and Wolford, M., 2017. Spectral and far-field broadening due to stimulated rotational Raman scattering driven by the Nike krypton fluoride laser. Applied optics, 56(31), pp.8618-8631.
[III.3] Lehmberg, R. H., C. J. Pawley, A. V. Deniz, M. Klapisch, and Y. Leng. "Two-photon resonantly-enhanced negative nonlinear refractive index in xenon at 248 nm." Optics communications 121, no. 1-3 (1995): 78-88.
[III.4] Betti, R., and O. A. Hurricane. "Inertial-confinement fusion with lasers." Nature Physics 12, no. 5 (2016): 435.
[III.5] Nibbering, E. T. J., G. Grillon, M. A. Franco, B. S. Prade, and André Mysyrowicz. "Determination of the inertial contribution to the nonlinear refractive index of air, N 2, and O 2 by use of unfocused high-intensity femtosecond laser pulses." JOSA B14, no. 3 (1997): 650-660.
[III.6] Lehmberg, R. H., J. Reintjes, and R. C. Eckardt. "Negative nonlinear susceptibility of cesium vapor around 1.06 μm." Physical Review A 13, no. 3 (1976): 1095.
[III.7] Grischkowsky, D., M. M. T. Loy, and P. F. Liao. "Adiabatic following model for two-photon transitions: nonlinear mixing and pulse propagation." Physical Review A 12, no. 6 (1975): 2514.
[III.8] Grischkowsky, D. "Coherent excitation, incoherent excitation, and adiabatic states." Physical Review A 14, no. 2 (1976): 802.
[III.9] Lehmberg, R. H., and S. P. Obenschain. Use of Induced Spatial Incoherence for Uniform Illumination on Laser Fusion Targets. No. NRL-MR-5029. Naval Research Lab, Washington DC, 1983.

[III.10] Lehmberg, R. H., A. J. Schmitt, and S. E. Bodner. "Theory of induced spatial incoherence." Journal of applied physics 62, no. 7 (1987): 2680-2701.
[III.11] Brabec, Thomas, and Ferenc Krausz. "Nonlinear optical pulse propagation in the single-cycle regime." Physical Review Letters 78, no. 17 (1997): 3282.
[III.12] Taha, Thiab R., and Mark I. Ablowitz. "Analytical and numerical aspects of certain nonlinear evolution equations. II. Numerical, nonlinear Schrodinger equation." Journal of Computational Physics 55, no. 2 (1984): 203-230.
[III.13] Crisp, M.D. "Adiabatic-Following Approximation." Physical Review A 8, no. 4 (1973): 2128.
[III.14] Junnarkar, Mahesh R., and Naoshi Uesugi. "Near-two-photon-resonance short-pulse propagation in atomic xenon." Optical Pulse and Beam Propagation. Vol. 3609. International Society for Optics and Photonics, 1999.
[III.15] Gornik, W., et al. "Two-photon excitation of xenon atoms and dimers in the energy region of the 5 p 56 p configuration." The Journal of Chemical Physics 75.1 (1981): 68-74.
[III.16] Bruce, M. R., et al. "Radiative lifetimes and collisional deactivation of two-photon excited xenon in argon and xenon." The Journal of chemical physics 92.5 (1990): 2917-2926.
[III.17] Grischkowsky, D. and Armstrong, J.A., 1972. Self-defocusing of light by adiabatic following in rubidium vapor. Physical Review A, 6(4), p.1566. [IV.1] D. Budker, W. Gawlik, D.F. Kimball, S.M. Rochwester, V.V. Yashchuk and A. Weis, Rev. Mod. Phys. 74, 1154 (2002).
[IV.2] Optical Magnetometry, D. Budker and D.F.J. Kimball (eds.) (Cambridge University Press, Cambridge, UK, 2013).
[IV.3] G. Bison, R. Wynands, and A. Weis, Appl. Phys. B Lasers Opt. 76, 325 (2003).
[IV.4] J.P. Davis, M.B. Rankin, L.C. Bobb, C. Giranda, M.J. Squicciarini, "REMAS Source Book," Mission and Avionics Tech. Dept., Naval Air Development Center (1989).
[IV.5] L. A. Johnson, P. Sprangle, B. Hafizi, and A. Ting. "Remote atmospheric optical magnetometry," Journal of Applied Physics, 116(6), (2014).
[IV.6] Z. Qiu and S. Bader, "Surface magneto-optical Kerr effect," Review of Scientific Instruments 71 (3), 1243-1255 (2000).
[IV.7] K. Oughstun and R. Albanese, "Magnetic field contribution to the Lorentz model," J. Opt. Soc. Am. A 23, 1751-1756 (2006).
[IV.8] J. D. Jackson, Classi cal electrodynamics. (Wiley, New York, 1999).
[IV.9] Andrei, E. 2015. Faraday Rotation [pdf]. Retrieved from:
http://www.physics.rutgers.edu/grad/506